IDEA League

Master of Science in Applied Geophysics

Research Thesis

# Enhancing Sweep Efficiency Assessment for $CO_2$ Plume Geothermal

## Tracer Field Campaign Recommendations on the Basis of Reservoir Simulations using Tagged $CO_2$

**Abigail Rhodes**

August 8, 2023

# Enhancing Sweep Efficiency Assessment for $CO_2$ Plume Geothermal

## Tracer Field Campaign Recommendations on the Basis of Reservoir Simulations using Tagged $CO_2$

Master of Science Thesis

for the degree of Master of Science in Applied Geophysics at
ETH Zürich
by

Abigail Rhodes

August 8, 2023

Department of Earth Sciences · ETH Zürich



Printed in Switzerland

IDEA LEAGUE
JOINT MASTER'S IN APPLIED GEOPHYSICS

Delft University of Technology, The Netherlands
ETH Zürich, Switzerland
RWTH Aachen, Germany

Dated: *August 8, 2023*

Supervisor(s):

Martin Saar

Jasper de Reus

Mahmoud Hefny

Committee Members:

Martin Saar

Jasper de Reus

Mahmoud Hefny

Florian Wellman

# Abstract

The $CO_2$ Plume Geothermal (CPG) Consortium was created in March 2023 to demonstrate the potential and technical feasibility of $CO_2$ Plume Geothermal at candidate sites in an integrated academic and industry synergistic collaboration. Following 12 years of theoretical CPG research, the consortium will execute a field demonstration in order to de-risk future commercial scale projects. Tracer campaigns performed during a field demonstration can provide information on how the plume evolves over time, which may be extrapolated in time and space to estimate the long-term, large-scale heat recovery potential for commercial CPG projects. Gas tracers, however, have not yet been employed for these purposes. Here we define the optimal tracer field campaign recommendations based on reservoir simulations of the Sleipner field in offshore Norway. We found that the determination of $CO_2$ plume development and sweep conformance was optimized using 7 tracers (N=7) in one-month intervals (dt=1). Additionally, we found that our homogeneous model possesses the largest sweep of the three models, as a uniform permeability permits greater flow of $CO_2$ at greater depths in the reservoir. Based on our results, we recommend injecting 35 kg (5 kg each) of 7 perfluorocarbon tracers over 5-6 hours in one-month intervals for determination of $CO_2$ plume development. However, for different reservoirs of interest, similar simulations, such as used in this study, should be run to identify a suitable number of tracers (N) and a suitable injection interval (dt) for determining $CO_2$ plume development and convergence for that site. From our findings, a tracer campaign would help reduce uncertainty in modelling, predictions and history-matching and improve understanding of sweep efficiency and long-term heat recovery. Tracer campaigns performed during a CPG pilot demonstration can then enhance the sweep efficiency assessment for a commercial $CO_2$ Plume Geothermal power plant.

# Acknowledgements

I'd like to formally thank my advisors, Dr. Martin Saar, Jasper de Reus, and Dr. Mahmoud Hefny, for their insights and guidance. I am tremendously grateful for the opportunity to conduct research within the Geothermal Energy and Geofluids group at ETH Zürich and to be a part of the Consortium Research Team, even if for a few short months. Additionally, I would like to acknowledge Serhat Kücük, Tsubasa Onishi, and Kevin Hau for their mentorship and expertise. Lastly, I would like to thank my parents for their endless support.

Swiss Federal Institute of Technology
August 8, 2023

Abigail Rhodes

# Dedication

for Martha, Gwen, Art & Carlton

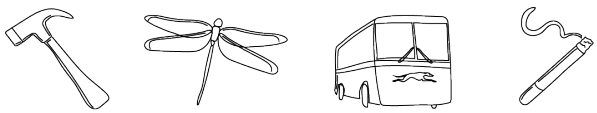

# Table of Contents

# List of Figures

# List of Tables

# Acronyms

**BECCS** Bio-Energy with $CO_2$ Capture and Storage

**BTC** Breakthrough curves

**CCS** Carbon Capture and Storage

**CMG** Computer Modelling Group Ltd.

**CPG** $CO_2$ Plume Geothermal

**DACCS** Direct Air $CO_2$ Capture and Storage

**EGS** Enhance Geothermal Systems

**EOR** Enhanced Oil Recovery

**FID** Final Investment Decision

**GHG** Greenhouse gases

**IWTT** Inter-Well Tracer Test

**PFT** Perfluorocarbons tracers

**s$CO_2$** Supercritical $CO_2$

**SINTEF** Stiftelsen for Industriell og Teknisk Forskning

**SWTT** Single-Well Tracer Test

**VOI** Value of Information

# Chapter 1

# Introduction

## 1-1 Motivation

$CO_2$ levels in the atmosphere are rising at an unprecedented rate, which could mean damaging consequences for ecosystems, agriculture, and human civilization at large (Shannon and Bielicki, 2021). In order to address this climate challenge, the Intergovernmental Panel on Climate Change recognizes Carbon Capture and Storage (CCS) as one of the necessary components (Metz et al., 2005). Renewables will also play a role in decarbonizing the future of electricity and heat production. Geothermal energy provides reliable, base-load power and is not susceptible to variable surface conditions like wind and solar. $CO_2$ Plume Geothermal (CPG) turns CCS into $CO_2$ Capture, Utilization and Sequestration (CCUS), utilizing $CO_2$ as a working fluid to extract geothermal energy while geologically sequestering 100% of the initially injected $CO_2$ eventually. By using $CO_2$ as a working fluid over brine, energy extraction rates are doubled to tripled. This finding assumes certain base case conditions, all else being equal. The CPG concept, developed theoretically by Prof. Saar, now necessitates real-world validation.

The CPG Consortium was created in March 2023 to demonstrate the potential and technical feasibility of $CO_2$ Plume Geothermal at candidate sites in an integrated academic and industry synergistic collaboration (GEG Group, 2023b). Following 12 years of theoretical CPG research and over 16 peer-reviewed journals (e.g. Adams et al. (2015a); Randolph and Saar (2011b,a); Randolph et al. (2012); Adams et al. (2013, 2014)) from Prof. Saar and his team, the CPG Consortium will execute a field demonstration in order to de-risk future commercial-scale projects to enable industry partners' Final Investment Decision (FID). Reservoir simulations can aid in derisking a commercial CPG power plant.

The shape of the $CO_2$ plume, or the volumetric sweep, over time determines the long-term heat recovery and, therefore, the success of a commercial CPG power plant. However, the plume develops hundreds of meters underground. So how can we determine the evolution

of $CO_2$ over time in such a hidden system? Methods such as numerical modeling (Norouzi et al., 2022), reservoir simulations (Olalotiti-Lawal et al., 2020), geophysical surveys (Equinor, 2020), and tracer campaigns (Myers et al., 2013) can assist in answering this question, using known rock and fluid properties. Tracer campaigns performed during a field demonstration can provide information on how the plume evolves over time, which may be extrapolated in time and space to estimate the long-term, large-scale heat recovery potential for commercial CPG projects. In this study we aimed to answer the following question,

> **How does varying the tracer injection interval (dt) and the number of tracers (N) in three reservoir models affect the determination of $CO_2$ plume development? What are the optimal tracer field campaign recommendations based on these reservoir simulations?**

In order to enhance sweep efficiency assessments and provide tracer field campaign recommendations, we use tagged $CO_2$ tracers in reservoir simulations. Gas tracers have been employed in studies for both carbon storage (Hassoun et al., 2000; Gilfillan et al., 2011; Myers et al., 2013; Melo et al., 2014) and geothermal (Ren et al., 2023), and tracers in general have been used extensively to investigate oil and gas flow in geologic reservoirs (Senum et al., 1992; Dugstad, 1992; Ljosland et al., 1993; De Reus et al., 2019). However, carbon storage studies typically recover tracers from a Single-Well Tracer Test (SWTT) or from the surface to detect leakages. Our tracer campaign will be novel as it injects and produces perfluorocarbon gas tracers in $CO_2$ in an Inter-Well Tracer Test (IWTT). Reservoir simulations aid in our understanding of this process.

During our study, we found that the determination of $CO_2$ plume development and sweep conformance was optimized using 7 tracers (N=7) in one-month intervals (dt=1). Additionally, we found that our homogeneous model possesses the largest sweep of the three models, as a uniform permeability permits greater flow of $CO_2$ at depth in the reservoir. Based on our results, we recommend injecting 35 kg (5 kg each) of 7 perfluorocarbon tracers (Perfluorocarbons tracers (PFT)) over 5-6 hours in one-month intervals. However, for different areas of investigation/reservoirs, similar simulations such as used in this study should be run to identify a suitable number of tracers and a suitable injection interval for determining $CO_2$ plume development and convergence for that site. We recommend sampling using the Agilent 6890N gas chromatograph until recovery of the peak and a portion of the exponential decay of the last tracer for optimal determination of $CO_2$ plume development. From our findings, a tracer campaign would help reduce uncertainty in modelling, predictions and history-matching and improve understanding of sweep efficiency and long-term heat recovery.

## 1-2 Problem: Climate Challenge

$CO_2$ levels in the atmosphere are rising at an unprecedented rate, which could mean damaging consequences for ecosystems, agriculture, and human civilization at large (Shannon and Bielicki, 2021).

> ***"The science is irrefutable: humans are altering our climate in ways that our economy and our infrastructure must adapt to... We can see the impacts of climate change around us every day. The relentless increase of carbon dioxide... is a stark reminder that we need to take urgent, serious steps to become [a] more Climate Ready [Nation]. "*** - Rick Spinrad, PhD, NOAA Administrator

While $CO_2$ is necessary to retain heat close to Earth's surface so the planet does not freeze over, increasing amounts of $CO_2$ may also be damaging to life as we know it (NASA Earth Science Communications Team, 2023). Recently, $CO_2$ levels have surpassed 400 ppm in the atmosphere (Figure 1-1).

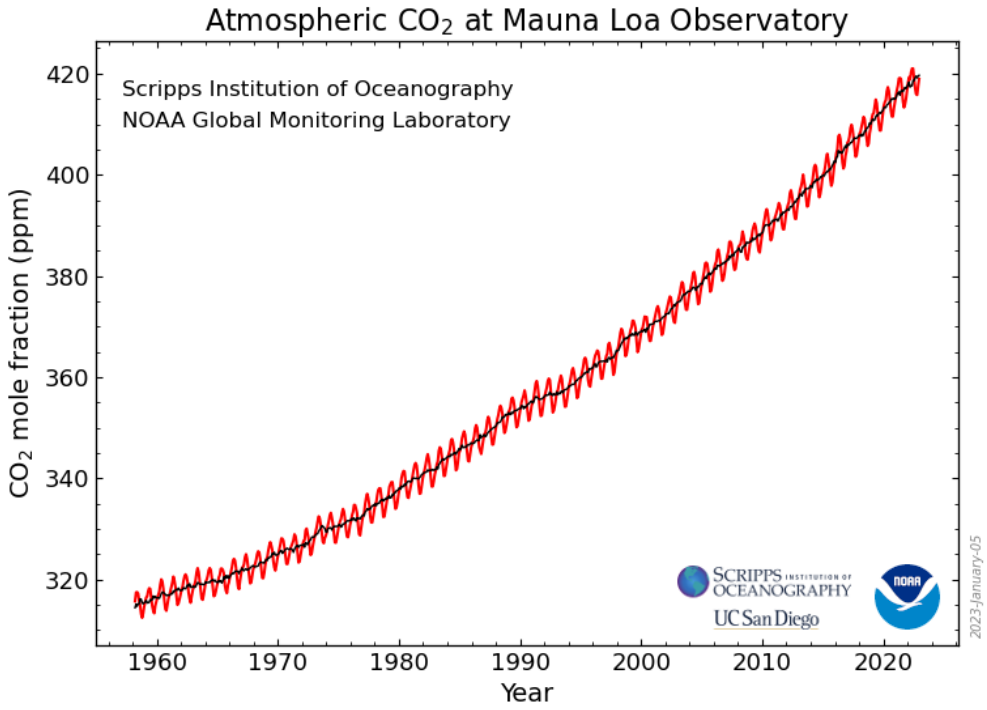


**Figure 1-1:** The Keeling curve displays the monthly mean carbon dioxide measured at Mauna Loa Observatory in Hawaii. The Keeling curve is the longest continuous recording of atmospheric $CO_2$. Oscillations reflect seasonal variations of $CO_2$ in the atmosphere.

The last time $CO_2$ levels were this high was 4.1 million years ago during the Pliocene Climactic Optimum (Stein, 2022). The geologic record shows that Earth's temperatures rise with increased atmospheric $CO_2$ concentration. This phenomena is attributed to something known as the greenhouse effect (Figure 1-2).

As solar radiation penetrates Earth's atmosphere, much of this heat is absorbed by the Earth. The heat that is not absorbed is reflected back towards space. Greenhouse gases (GHG) such as $CO_2$ serve to trap that heat in Earth's atmosphere. Not all of the heat is trapped, however. It is important for some heat to remain in the atmosphere so the planet does not freeze over, however, increasing amounts of $CO_2$ increase the amount of heat that is trapped. Warmer temperatures on Earth induce a positive feedback loop, whereby, warming oceans release more stored $CO_2$ into the atmosphere, which warms the atmosphere, which warms the oceans, which release more $CO_2$ ... and the cycle continues (NASA Earth Science Communications Team, 2023).

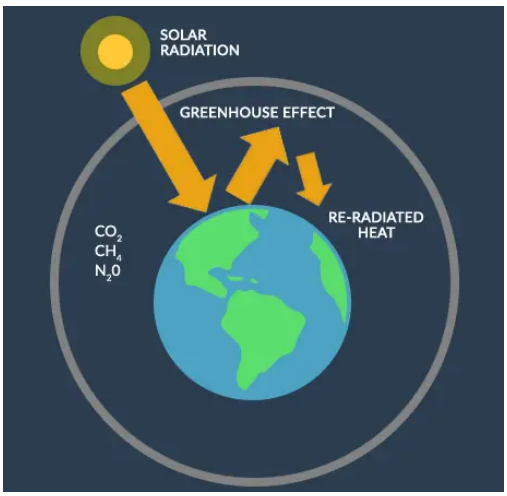


**Figure 1-2:** Greenhouse gas effect on Earth. With the presence of greenhouse gases, such as carbon dioxide ($CO_2$), methane ($CH_4$), and nitrous oxide ($N_2O$), solar radiation is trapped in Earth's atmosphere (EarthHow, 2022)

Due to the accelerated rate at which $CO_2$ is being released into the atmosphere, our climate does not yet reflect the temperatures we might expect with our current atmospheric composition. Due to this climactic lag, we have not yet realized the full consequences of global warming. During the Pliocene Climactic Optimum, when $CO_2$ levels were last above 400 ppm, sea levels were between 5 and 25 meters higher than they are today. Sea level rise of this magnitude today would drown many of the world's largest cities and displace millions of people (Dumitru et al., 2019). During the Climactic Optimum, glaciers were depleted, polar regions warmed, and large forests occupied the modern-day Arctic tundra (Brigham-Grette et al., 2013). This sudden shift in atmospheric composition will contribute to ocean acidification, migration of disease carrying insects, and extreme weather events (Stein, 2022).

**Figure 1-3:** Devastation from the March 31st, 2023 tornado that struck capitol-city Little Rock in Arkansas (USA) (Albarado and Grajeda, 2023)

**Droughts, flooding, tornadoes, wildfires, tropical storms...**

These are all weather events we can expect with greater frequency and severity as our climate catches up to atmospheric $CO_2$ levels. The jet stream is a major contributor to the circulation of warm and polar air. The temperature difference at the poles and the equator keeps the jet stream stable and balanced as seen on the left side of Figure 1-4. The temperature gradient serves to channelize the jet stream much like a river might flow from high elevation to low elevation. However, increased temperatures at the poles result in a smaller temperature difference between the poles and the equator, forcing the jet stream to meander in an unstable configuration as seen on the right side of Figure 1-4. The destabilization generates situations of extreme weather at midlatitudes such as heat waves, hurricanes, and tornadoes (Fonseca et al., 2022). Tornadoes result from unstable weather conditions where warm, humid air collides with cool, sinking air, producing a rotating column of air. Such favorable conditions for tornadoes exist in the central United States in an area colloquially referred to as Tornado Alley seen in red in Figure 1-5. Here, the warm moist air from the Gulf of Mexico combines with the cold-dry air from Canada and northern parts of the United States. Tornado frequency and severity will only increase, and is projected to shift eastward into states such as Missouri and Arkansas (DeMillo, 2023).

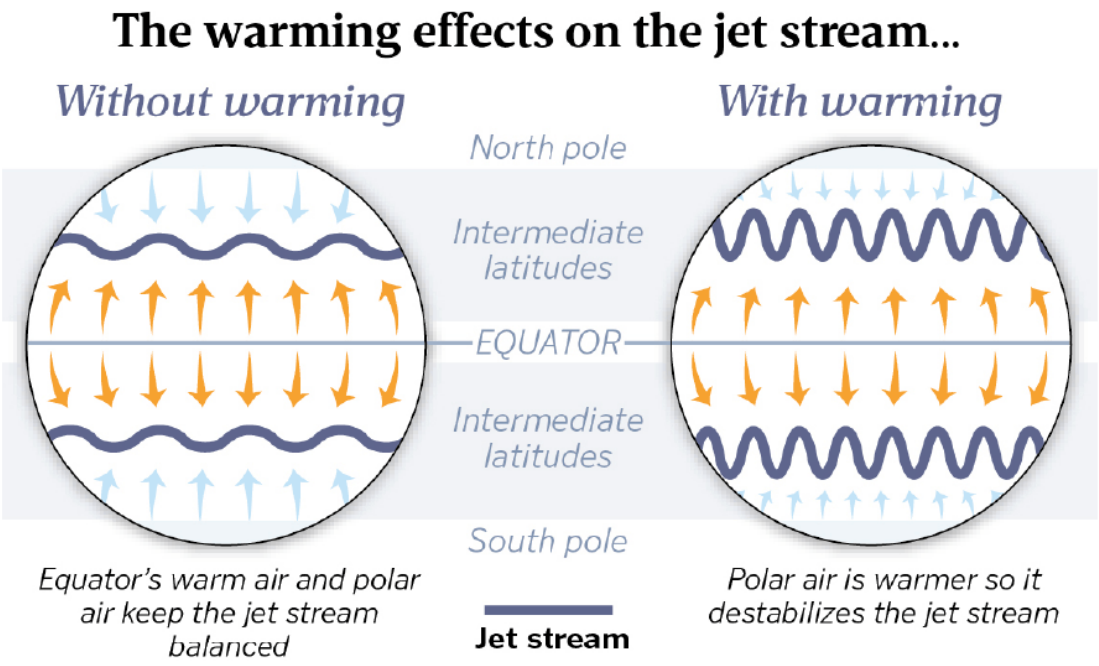


**Figure 1-4:** The warming effects on the jet stream. Increased temperatures at the poles force the jet stream to meander with a greater amplitude in an unstable configuration. This destabilization generates situations of extreme weather at midlatitudes (Fonseca et al., 2022).

> ***"Climate projections for the late 21st century have suggested that the conditions favorable to the development of the severe storms that produce tornadoes will increase over North America."*** - John T. Allen, Professor of Meteorology at Central Michigan University (Treisman, 2023)

During the drafting of this thesis, a tornado struck my hometown of Little Rock, Arkansas, in the United States in March 2023, damaging thousands of homes and businesses and killing five people. Hundreds of families were displaced and property damage was tremendous. Even my family experienced some damages to our home. Climate-based natural disasters kill thousands of people per year and shake the lives of many more. The occurrence of severe weather events such as tornadoes will only increase in the future in addition to the millions of people that will be displaced by rising sea levels. In order to lessen the changing climate's impacts to life as we know it, humans must reduce our $CO_2$ emissions to the atmosphere or find other ways to prevent carbon dioxide from remaining in the atmosphere.

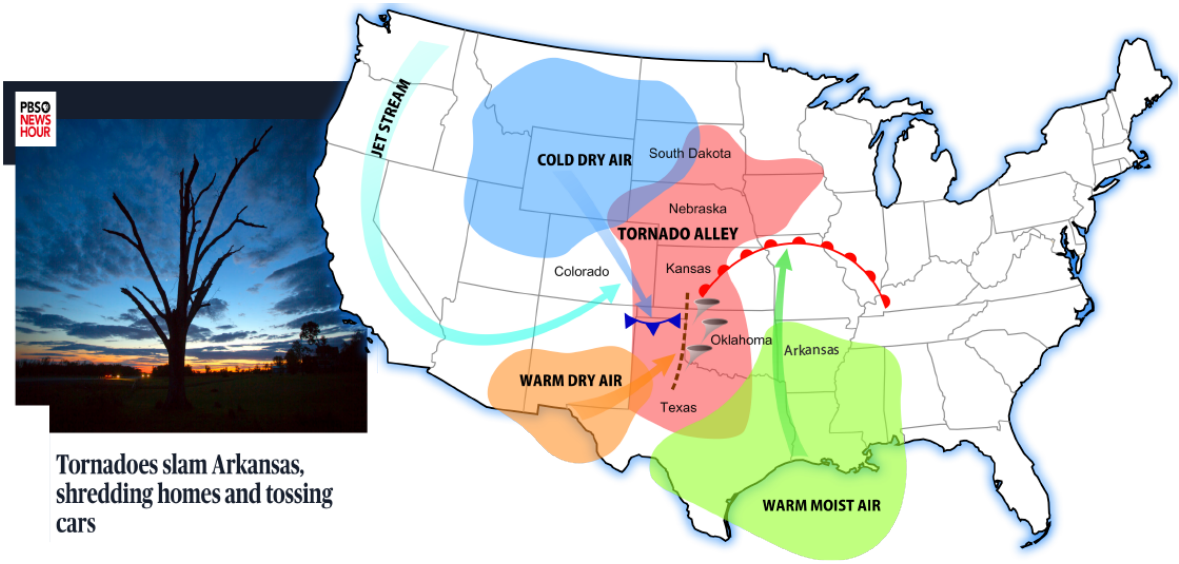


**Figure 1-5:** PBS news article from March 31st tornado in Arkansas DeMillo (2023) and diagram of tornado alley (Wiki Authors, 2023). In the article, author Andrew DeMillo of the Associated Press and PBS expalains, "a tornado raced through Little Rock and surrounding areas Friday, splintering homes, overturning vehicles and tossing trees and debris on roadways as people raced for shelter." The diagram showing tornado alley forms as the warm moist air from the Gulf of Mexico combines with the cold-dry air from Canada and northern parts of the United States.

### 1-2-1 Solution: Carbon Storage

The Intergovernmental Panel on Climate Change recognizes carbon storage as one of the necessary components for tackling the modern day climate challenge (Metz et al., 2005).

Carbon Storage (CS) is commonly discussed within the context of the joint process of Carbon Capture and Storage (CCS), whereby $CO_2$ is captured directly from a source, transported, and stored geologically underground. $CO_2$ is captured at point-source $CO_2$ emitters such as power plants, cement manufacturers, or bio-fuel refineries. In this process, the $CO_2$ that otherwise would have entered the atmosphere is diverted and stored geologically. Therefore, Carbon Storage alone is classified as a $CO_2$-neutral process, not $CO_2$-negative. However, $CO_2$-negative processes do exist such as Bio-Energy with $CO_2$ Capture and Storage (BECCS) or Direct Air $CO_2$ Capture and Storage (DACCS). In BECCS, $CO_2$-absorbing biomass is burned for energy and the resulting $CO_2$ from the gas is stored underground. In this process, $CO_2$

is absorbed, produced, and stored. The absorption allows this process to be $CO_2$-negative. In DACCS, $CO_2$ is captured from ambient air and not from a point source. It is then stored geologically underground. The $CO_2$ that is captured could have a range of sources and is not associated with any one point-source $CO_2$ emitter. Thus, the process seeks to reduce general $CO_2$ in the atmosphere in a $CO_2$-negative process. One example of DACCS is the implementation of a direct-air $CO_2$ capture technology from Swiss-based Climeworks in Iceland in a partnership with CarbFix that stores the captured $CO_2$ in basaltic rock. The stored $CO_2$ mineralizes in the basaltic rock over time for high-security storage. The process is shown below in Figure 1-6.

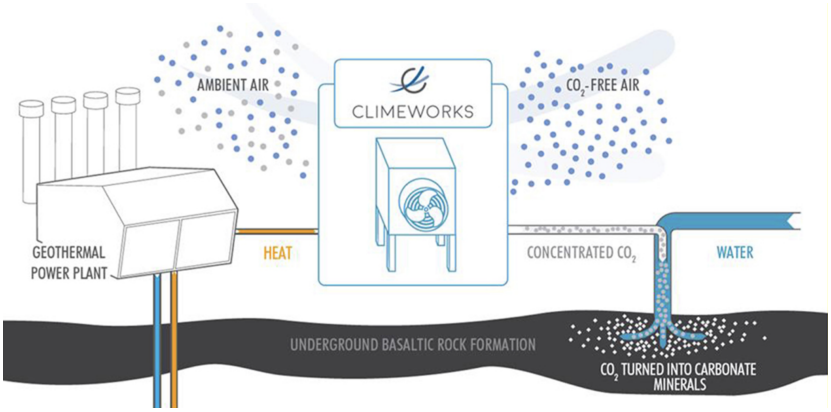


**Figure 1-6:** Diagram of joint Climeworks direct air capture and Carbfix carbon storage technologies in Iceland (Wilcox et al., 2019).

While many technologies exist for capturing $CO_2$, this thesis is concerned more with geologic $CO_2$ storage. Above in Section 1-2 we discussed how greenhouse gases serve as a trapping mechanism for heat from solar radiation. Similarly, the subsurface may be used as a trapping mechanism for $CO_2$. In order for $CO_2$ to be permanently stored underground, physical trapping mechanisms must first be in place, namely, stratigraphic and structural trapping. Stratigraphic trapping refers to a porous, permeable layer that is bounded on top by an impermeable or low-permeability layer that prevents fluids from "leaking", or travelling upwards due to the buoyancy of the fluid. A structural trap refers to the geologic "structure" that traps the fluids within the permeable layer, either through an anticline or a fault as demonstrated in Figure 1-7.

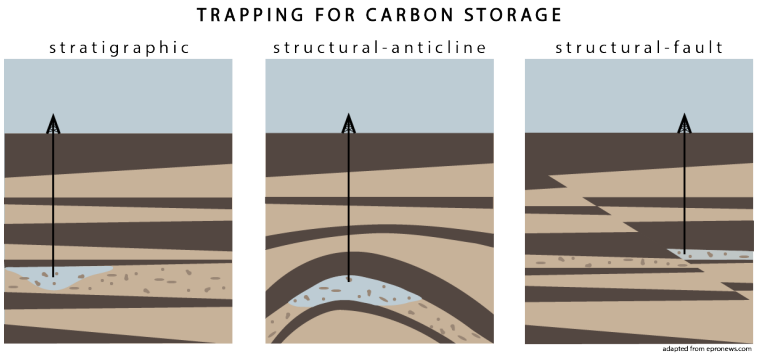


**Figure 1-7:** Structural and stratigraphic trapping mechanisms

Once $CO_2$ undergoes structural and stratigraphic trapping, residual $CO_2$ trapping occurs, whereby the migrated $CO_2$ plume leaves behind residual $CO_2$. Over time, the residual $CO_2$ dissolves in the brine. However, the rate of dissolution is highly dependent on the temperature, pressure, and salinity of the solution (Spycher et al., 2003; Spycher and Pruess, 2010). Additional processes such as diffusion and convection of $CO_2$ and density-driven flow affect the $CO_2$ storage security during residual and solubility trapping. As $CO_2$ dissolves into the water, the water becomes denser than the surrounding water into which no $CO_2$ has yet dissolved and sinks. As a result, viscous fingering occurs. In Figure 1-8 we see two fingering regimes resulting from two different permeability fields.

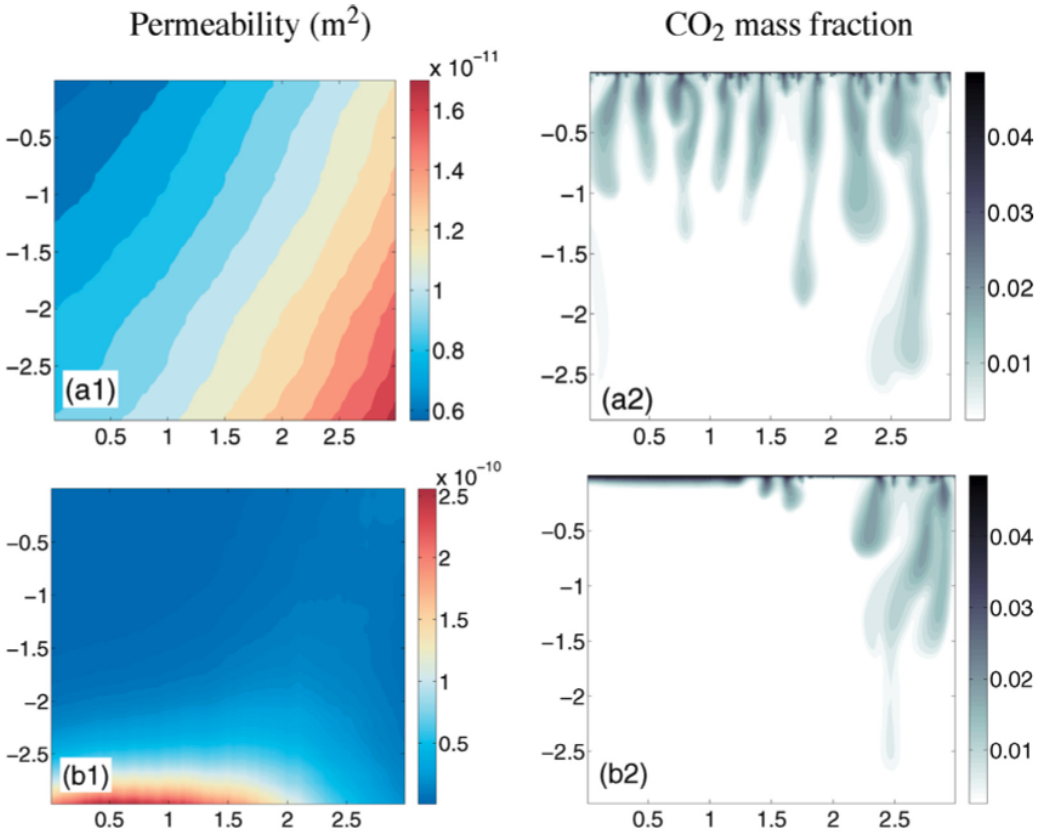


**Figure 1-8:** $CO_2$ dissolution fingering regimes based on permeability fields: (a) unbiased-fingering regime and (b) preferential-fingering regime (Kong and Saar, 2013).

Over the course of hundreds of years, the $CO_2$ mineralizes, thereby forming a carbonate rock, such as a limestone. Through the mineralization process, the $CO_2$ becomes virtually permanently trapped. In Figure 1-9 this can be visualized. Here, we see the contribution of each type of trapping mechanism starting from the initial injection of $CO_2$. The relative importance of these varies with time. With time, $CO_2$ becomes increasingly stored by residual then solubility then mineral trapping mechanisms. With each type of trapping mechanism in place, $CO_2$ storage security increases. While the final forms of geochemical trapping happen on the scale of hundreds to thousands of years, the leakage risks decrease with time. Carbon storage is different from nuclear storage in this way in that storage improves with time. $CO_2$ has been fully stored once it has mineralized.

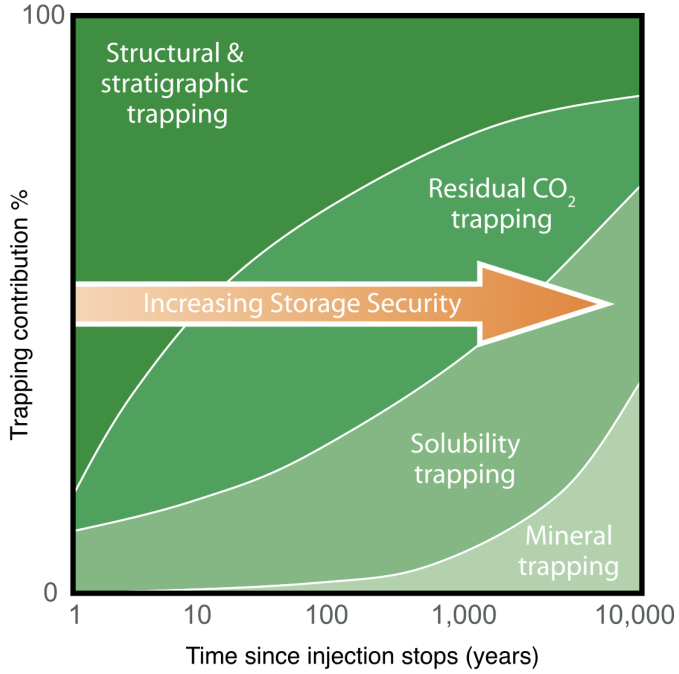


**Figure 1-9:** Contribution of the four trapping mechanisms (stratigraphic/structural, residual, solubility, and mineral) in storing $CO_2$ over thousands of years after injection (Metz et al., 2005).

## 1-2-2 Site Selection

In order for a site to be suitable for $CO_2$ storage, the following criteria must be in place,

1. physical and/or geochemical traps
2. point-source $CO_2$ emitters for $CO_2$ storage
3. adequate $CO_2$ storage capacity
4. sufficient reservoir permeability
5. no $CO_2$ leakage pathways

Any potential leakage of $CO_2$ to the surface is important to monitor. Faults, thin impermeable layers, and abandoned wells introduce regions of higher permeability and potential leakage pathways. Risk of leakage decreases on the scale of hundreds of years as seen in Figure 1-9. Thus, monitoring is necessary during the early stages when leakage risks are the greatest. $CO_2$ leakage may be monitored through the use of geophysical surveys or tracer campaigns. The monitoring of $CO_2$ migration and accumulation in the Utsira formation at the Sleipner field in offshore Norway is seen in Figure 1-10. Here, any leakage to the surface would likely also be visible.

While CCS will contribute to reducing the amount of $CO_2$ released into the atmosphere, renewable energy technologies, such as geothermal, will also be important for reaching future climate goals (Pacala and Socolow, 2004).

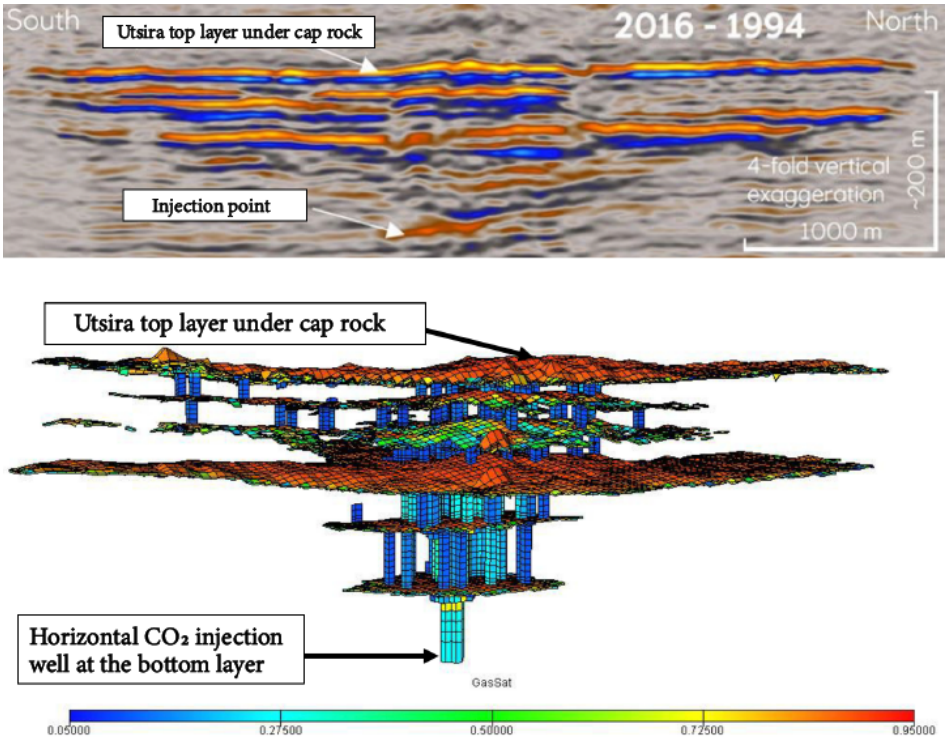


**Figure 1-10:** $CO_2$ accumulation from seismic survey (top) (Equinor, 2020) and pathways from modelling (bottom) (Akervoll et al., 2009) in the Utsira formation of the Sleipner field in offshore Norway. A caprock overlies the formation, preventing $CO_2$ leakage to the surface. The presence of a $CO_2$ leak through the caprock would likely be visible in such a seismic section.

### 1-2-3 Solution: Geothermal

Geothermal energy uses the heat from the Earth to heat homes or to produce electricity. Geothermal energy provides reliable, base-load and dispatch-capable power and is not susceptible to variable surface conditions like wind and solar energy. Because the heat in the subsurface regenerates, geothermal energy is renewable, clean, and continuous (Towler, 2014). The heat within the Earth is derived from two main sources. The first being heat created during the formation of the Earth. The second is attributed to the decay of radioactive elements, most notably Uranium, Thorium, and Potassium. Radioactive decay accounts for the majority of the heat within the crust. We can see the temperature-depth profile of the Earth in Figure 1-11. The geothermal gradient varies based on the layer of Earth with a much shallower geothermal gradient in the lithosphere, about 25°C/kilometer. Geothermal exploration utilizes heat from the shallow subsurface down to a few kilometers. Heat pumps may be used underneath homes and buildings to heat and cool the buildings. For electricity generation, deep wells are drilled into the subsurface. However, the temperature gradient, permeability, and ease of fluid flow in reservoirs is highly variable. Thus, the following geothermal energy generation technologies exist.

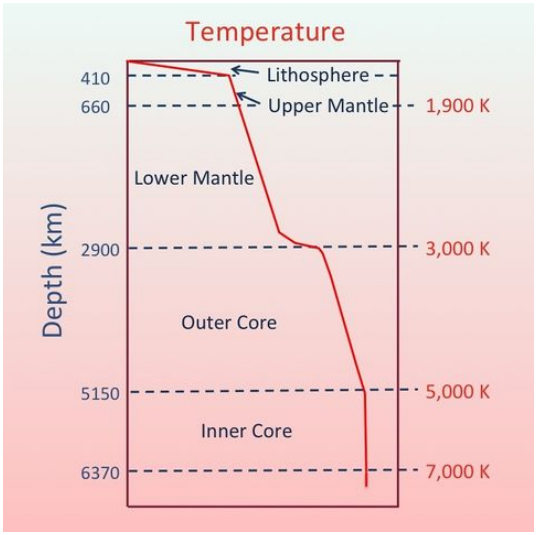


**Figure 1-11:** Temperature-depth profile of Earth (University of Calgary, 2023)

1. Hydrothermal
2. Enhanced Geothermal System (EGS)
3. Advanced Geothermal System (AGS)
4. $CO_2$ Plume Geothermal (CPG) systems

**Hydrothermal systems**, which are most of the geothermal systems in existence, utilize the natural permeability and fluid flow within a high to moderate-temperature system. **EGS or petrothermal systems** improve fluid flow through hydrofracturing. This technology is not yet mature and exists in only two places at the moment, at Soultz in the Rhine Graben and at Gross Schönebeck. This technology would expand the amount of geothermal resource we are able to exploit by artificially enhancing the pre-existing low permeability. **Advanced geothermal systems (AGS)** are also a novel technology, utilizing a closed loop, however. Hydraulic stimulation is not involved in this drilling method. The working fluid is instead heated within the pipe by conduction with the surrounding hot rock (GEG Group, 2023a). We can see a comparison of these three systems in Figure 1-12. Notably we see the depth of geothermal targets for each and, consequently, the required drilling depth. Hydrothermal

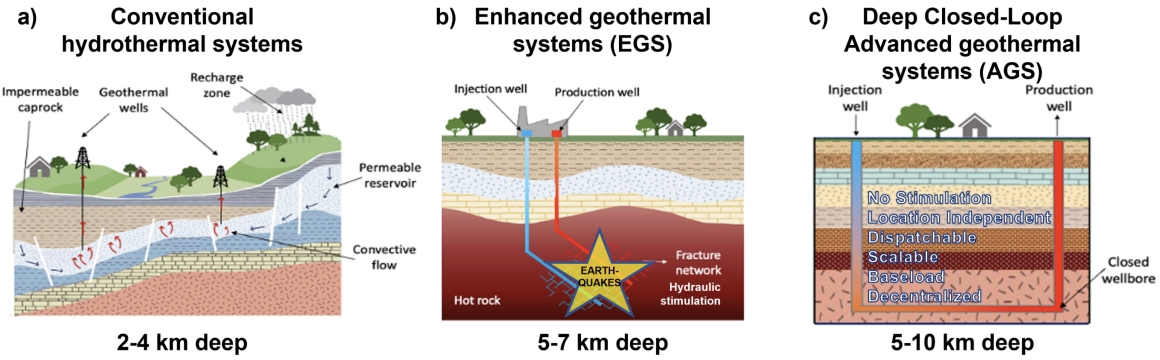


**Figure 1-12:** Geothermal system types: (a) Conventional hydrothermal systems. (b) Enhanced geothermal systems. (c) Deep closed-loop advanced geothermal systems (GEG Group, 2023a)

utilizes the shallowest targets and AGS, the deepest. The figure identifies the advantages of AGS – no stimulation is required, the system is location independent, power is dispatchable, the system is scalable, baseload power is produced, and the system is decentralized. However, the method is still in its infancy. Lastly, **$CO_2$ plume geothermal** (Figure 1-13) utilizes high porosity and permeability, shallow, and medium to low heat reservoirs and uses $CO_2$ as opposed to water as a working fluid (GEG Group, 2023b). The CPG concept, developed theoretically by Prof. Saar, now necessitates real-world validation. Below, we describe the benefits of using $CO_2$ as a working fluid and the concept of CPG more in depth.

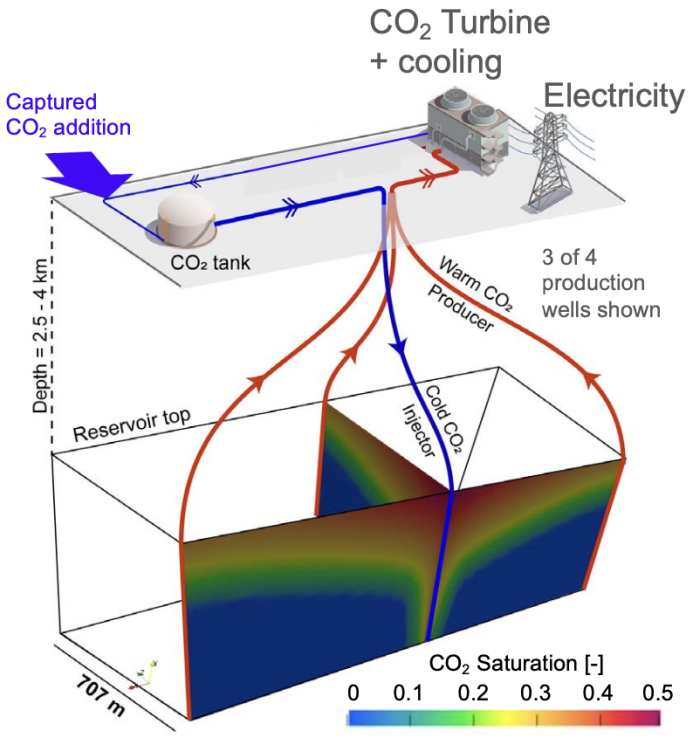


**Figure 1-13:** $CO_2$ plume geothermal system

# Chapter 2

# Background

## 2-1 $CO_2$ Plume Geothermal (CPG)

Brown at Los Alamos National Laboratory in the United States first illustrated the benefits of using Supercritical $CO_2$ ($sCO_2$) as a working fluid for Enhance Geothermal Systems (EGS) in 2000. $CO_2$ has a large density difference between its cold and warm supercritical states, with cold $CO_2$ being twice as dense as warm $CO_2$ under certain conditions. In the study, for an injection pressure of 30 MPa at 40°C and a surface production backpressure of 30 MPa at 250°C, the cold $CO_2$ (0.96 g/cc) was more than twice as dense as the warm $CO_2$ (0.39 g/cc). This difference in density causes a pressure differential pushing fluid through the reservoir and toward the production well (Pruess, 2006).

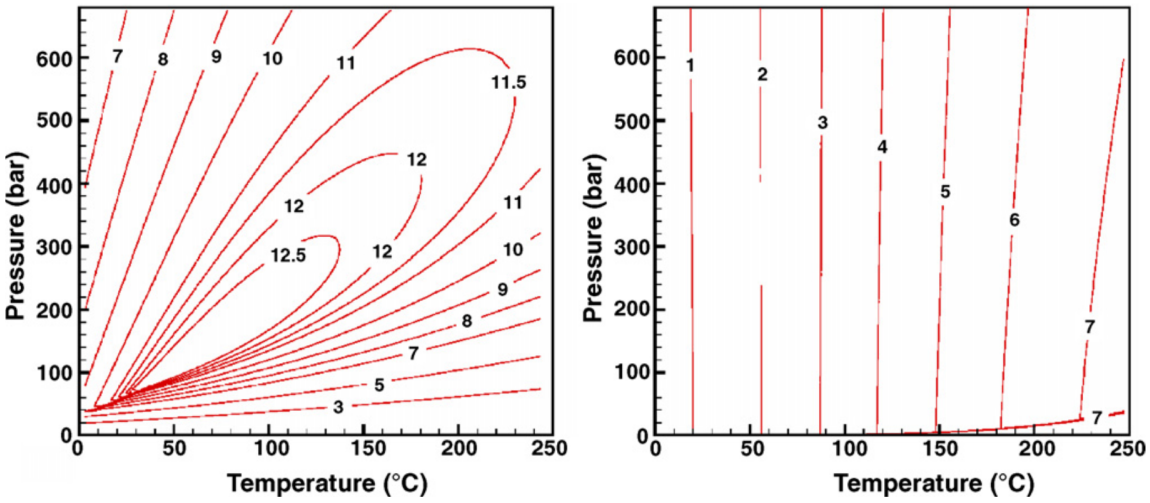


**Figure 2-1:** Ratio of fluid density to viscosity ($\frac{\rho}{\mu}$), the inverse of kinematic viscosity ($\frac{\mu}{\rho}$) which is discussed later, for $CO_2$ (left) and water (right) measure in $\frac{s}{m^2}$ (Pruess, 2006)

In Figure 2-1, we see that the ratio of fluid density to viscosity of water (right) is extremely sensitive to changes in temperature. That means, for a slight increase in temperature the fluid either becomes more dense, more mobile, or a combination of both. $CO_2$ is also sensitive to changes in temperature as well as pressure. The largest values of the density to viscosity ratio for $CO_2$ are seen at intermediate temperatures and pressures. Here we would also have the smallest values of kinematic viscosity, as this is the inverse of the density to viscosity ratio. Density differences cause a buoyancy force as cold $CO_2$ forces hot $CO_2$ up towards the production well in a thermosiphon effect. This can double the production flow rate and significantly reduce parasitic pumping power (Pruess, 2006).

From 50 - 100°C and 150-250 bar, $CO_2$ is extremely dense, or mobile, or a combination of both as $CO_2$ would be in its supercritical phase. Around 73.7646 bar (72.8 atm) and 31°C (304 K), gaseous $CO_2$ becomes supercritical. These pressure and temperature constraints occur typically around 800 meters depth. The temperature, pressure, and depth dependence for $CO_2$ phase can be visualized in Figure 2-2. At this depth, $CO_2$ has a density of 3.8 g/m$^3$ as compared to 100 g/m$^3$ at the surface. Past 800 meters, g/m$^3$ density remains fairly constant as temperatures and pressures continue to increase with depth.

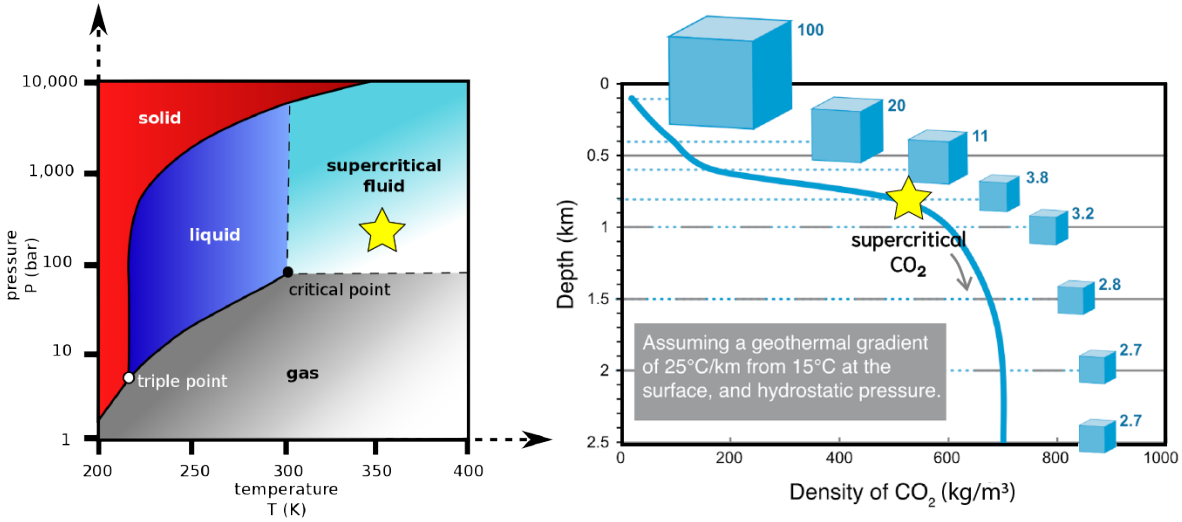


**Figure 2-2:** $CO_2$ phase diagram (left) and $CO_2$ depth-density relationship (right) from Metz et al. (2005). The cubes represent the relative volume occupied by $CO_2$, beginning with an initial volume of 100 m$^3$. $CO_2$ reaches a supercritical state around 73.7646 bar (72.8 atm) and 31°C (304 K), occurring at approximately 800 meters depth.

Brown also remarked on the inability of $CO_2$ to transport or precipitate mineral species as water can. Thus, issues such as scaling in pipes or changes in reservoir permeability associated with using water as a working fluid are not a problem when using $CO_2$ (Pruess, 2006). These early papers emphasized $CO_2$'s low kinematic viscosity which could double the production flow rate compared to that of water, despite the higher heat capacity of water. This is addressed more in depth later in the report. Pruess of Berkeley National Laboratory substantiated this claim in 2007 when he found that there are larger fluid extraction rates for $CO_2$ than for water for the same applied pressure in injection and production wells (Pruess, 2007)).

### 2-1-1 Advent of $CO_2$ Plume Geothermal

The development of $CO_2$-based geothermal saw major progress as Randolph and Saar (2011) introduced the $CO_2$ Plume Geothermal (CPG) concept which couples carbon sequestration and geothermal energy production, thereby improving the economic viability of carbon capture and storage and widening the application to moderate/low-temperature geologic reservoirs. We see in Figure 2-3b the process of CPG, where cold $CO_2$ is injected from the surface in an inverted 5-spot well configuration (Figure 2-3a). As the $CO_2$ flows outwards and is heated, the supercritical (but gas-like) $CO_2$ plumes upwards and moves up the production well back to the surface. At the surface, the produced $CO_2$ is directly expanded in a turbine, cooled, and re-injected into the subsurface. The turbine powers a generator which generates electricity for the grid.

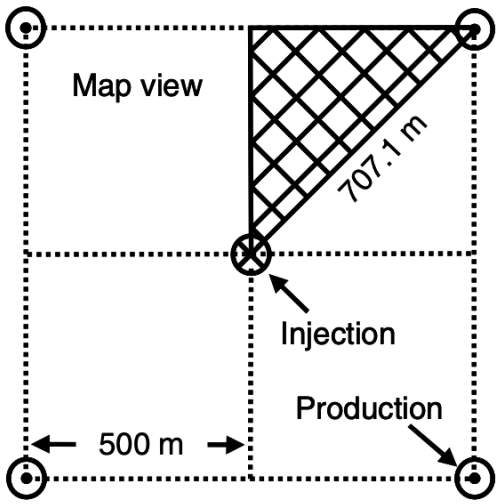


**(a)** 5 spot well configuration with injection well in the center and four surrounding production wells

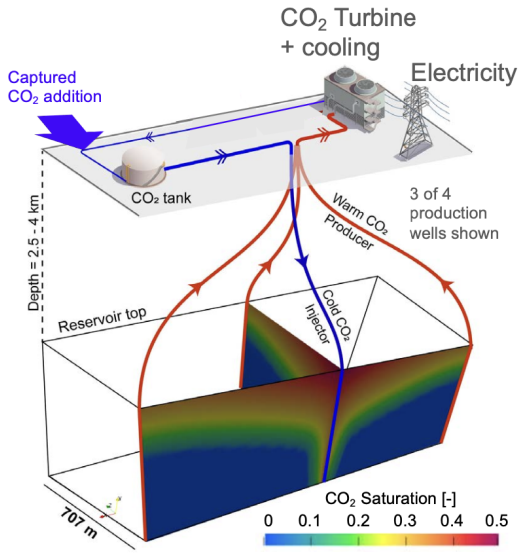


**(b)** Diagram of $CO_2$ Plume Geothermal and $CO_2$ saturation level

Instead of focusing on enhanced/engineered geothermal systems that utilize hydrofracturing of hot dry rock to enhance permeability, Randolph and Saar shifted their focus to naturally high porosity and high permeability, shallower reservoirs. Hydrofracturing is met with great resistance as citizens worry about induced seismicity. Not only is it more socially acceptable and environmentally safe to avoid hydrofracturing, but naturally high porosity and permeability reservoirs tend to be larger than hydrofractured reservoirs which improves $CO_2$ sequestration potential. Additionally, using shallower, moderate to low temperature reservoirs, would widen the applicability of carbon capture utilization and storage (CCUS) efforts. For example, in the United States many of the areas of moderate to high subsurface temperature (Figure 2-4) correspond to sedimentary basins that might be utilized for $CO_2$ sequestration in addition to geothermal energy generation. Such locations might be suitable for $CO_2$ Plume Geothermal.
They additionally found $CO_2$ to have heat extraction rates up to 3 times greater than those

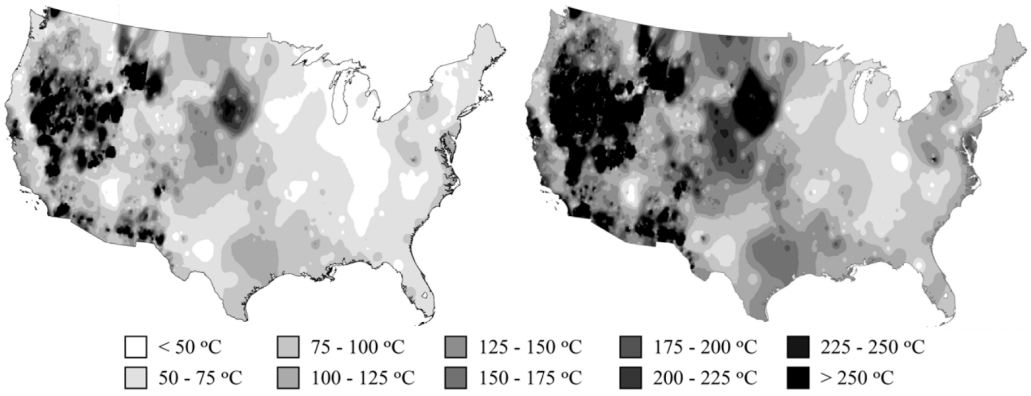


**Figure 2-4:** Shallow temperature maps of the USA at 2.5 km (left) and 4 km (right) depth.

of water-based systems (Figure 2-5), adding to the advantages of using $CO_2$ as a working fluid (Adams et al., 2014).

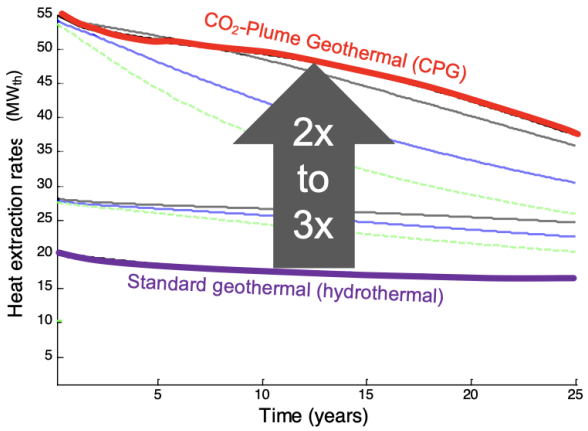


**Figure 2-5:** Heat extraction rates over time for $CO_2$ Plume Geothermal (red), standard geothermal (hydrothermal) (purple) and enhanced geothermal systems with various thicknesses and permeabilities.

### 2-1-2 Kinematic Viscosity

Further research was conducted in 2014 to identify more benefits of $CO_2$ as a working fluid. Adams et al. made the following conclusions:

1. $CO_2$ generates larger self-convecting mass flow rates than brine in indirect power cycles
2. $CO_2$ can extract heat faster than brine at shallower depths (0.5 – 1.5 km in this study)
3. $CO_2$ can use a greater fraction of extracted heat for pumping
4. $CO_2$ has large density changes with small temperature changes making it especially advantageous over water at depths from 0.5 to 3 km.

5. $CO_2$ has a smaller Darcy flow-induced pressure drop than water

All of these benefits reduce the parasitic pumping power commonly required for water-based geothermal systems (Adams et al., 2014). Expanding on Item 5, Darcy flow produces a pressure drop in the circulating fluid between the injection and production wells which can be represented as follows.

$$\Delta P = [\frac{\mu L}{\rho \kappa A}] * \dot{m} \tag{2-1}$$

We can further simplify the bracketed portion to represent the average specific inverse mobility $M$. Previously this was referred to as the inverse of our density to viscosity ratio.

$$M = [\frac{\mu L}{\rho \kappa A}] \tag{2-2}$$

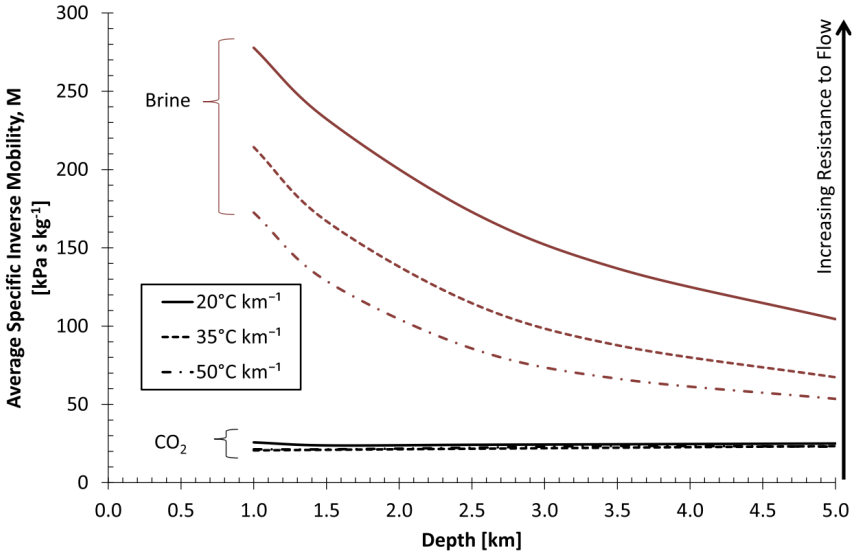


**Figure 2-6:** Average specific inverse mobility, $M$, for brine and $CO_2$ at different depths (Adams et al., 2014)

where $\mu$ is the dynamic viscosity $[\frac{kg}{m*s}]$, $L$ is the length between the injection and production wells $[m]$, $\rho$ is the density of the fluid $[\frac{kg}{m^3}]$, $\kappa$ is the permeability of the reservoir $[m^2]$, $A$ is the cross-sectional area $[m^2]$, and $\dot{m}$ is the fluid mass flow rate $[\frac{kg}{s}]$. $M$ can also be seen as a product of the kinematic viscosity $\frac{\mu}{\rho}$ and reservoir properties $\frac{L}{\kappa A}$ and represents how the reservoir and fluid properties resist flow.

$CO_2$ has a lower average specific inverse mobility than water at depths shallower than 5 km for various thermal gradients (Figure 2-6). This advantageously reduces the pressure drop and therefore the required pumping power. Additionally, M is mostly constant for $CO_2$ as temperature changes in the subsurface, however, the density of water is sensitive to changes in temperature as also seen in Figure 2-6, resulting in greater pressure drops with decrease in temperature.

In this way, $CO_2$ is more robust and outperforms brine in mass flow rate and heat extraction (Adams et al., 2014). These advantages are particularly beneficial at depths from 0.5 to 3 km. $CO_2$ also produces more electric power than brine at lower permeabilities as demonstrated in Figure 2-7 (Adams et al., 2015b).

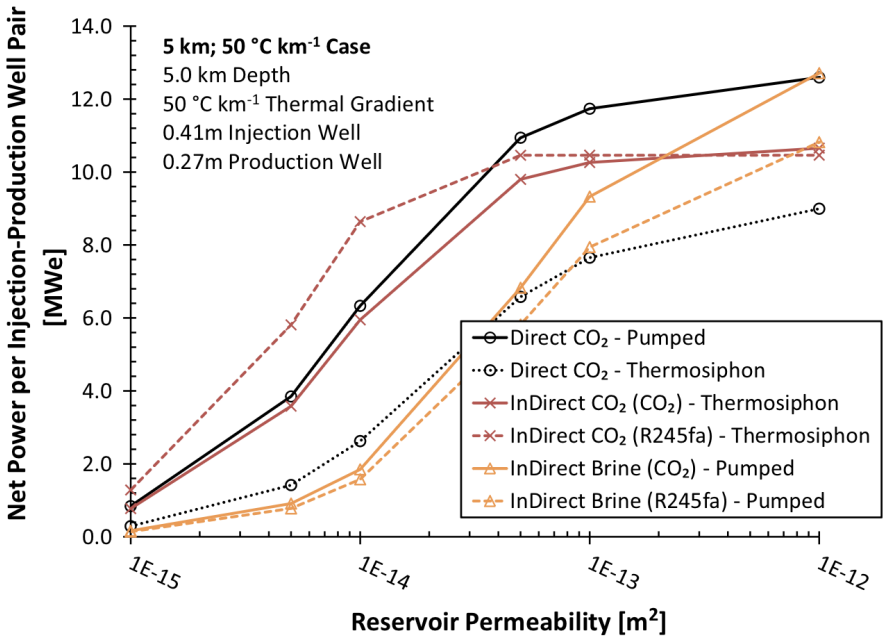


**Figure 2-7:** Net Power per Injection-Production Well Pair in response to Reservoir Permeability for six different geothermal systems. Systems utilized either $CO_2$ or brine as a working fluid in a direct or indirect system using purely a thermosiphon or pumping for production of the fluid.

Seen here, direct $CO_2$ – Pumped outperforms all brine systems in net power per injection-production well pair [MWe] at permeabilities less than $1 * 10^{-}12m^2$. In this case, they assume a depth of 5 km and a thermal gradient of 50°C/km. Later studies also revealed that the presence of water in the $CO_2$ fluid is not a major issue. Water-saturated $CO_2$ increases the turbine electric power output up to 41% compared to dry $CO_2$ (Fleming et al., 2020).

## 2-2 Tracers

### 2-2-1 What are Tracers?

Tracers are chemicals or other substances placed in or around the borehole to measure fluid movement between wells (Schlumberger Limited., 2023).

**active, passive, natural, artificial . . .**

There are many classifications and applications for tracers, and here we seek to break down the classification scheme. Active, or non-conservative, tracers interact with other fluids or the rock matrix through processes such as adsorption. Adsorption refers to the adherence of fluid molecules onto a rock substrate in the subsurface. For example, dye has strong sorptive tendencies. Heat is another example of a non-conservative tracer as heat can be lost to the system and is therefore poorly conserved. Partitioning tracers have an affinity for multiple phases and behave reactively after partitioning between two or more phases. Passive, or conservative, tracers passively follow the fluid in which it is injected with no interaction with reservoir materials. Inert tracers do not react with chemicals in the reservoir; novel or adsorptive tracers do react. Natural tracers are substances that occur naturally in the system and heightened concentrations may reflect a property of the subsurface. Artificial tracers are ones that are injected by the investigator for a specific purpose.

### 2-2-2 What are Tracers Used For?

Tracers are used in hard to image areas. This is not dissimilar to geophysical methods. Luhmann et. al. uses multiple tracers to model the flow path of a cave system (Luhmann et al., 2012), and tracers have also been used to take measurements inside a buried pipe (Hassoun et al., 2000) or inside the human body (Hamilton, 1942). Tracers are used widely in geothermal studies, hydrogeology, and petroleum engineering. In the oil and gas industry tracers are used to determine residual oil saturation and effectiveness of water sweep for Enhanced Oil Recovery (EOR) (Myers et al. (2013); Ljosland et al. (1993)). A visualization of sweep efficiency can be found below in Figure 2-8.

**Volumetric sweep efficiency: A measure of the effectiveness of an enhanced oil recovery process that depends on the volume of the reservoir contacted by the injected fluid** (Schlumberger Limited., 2023)

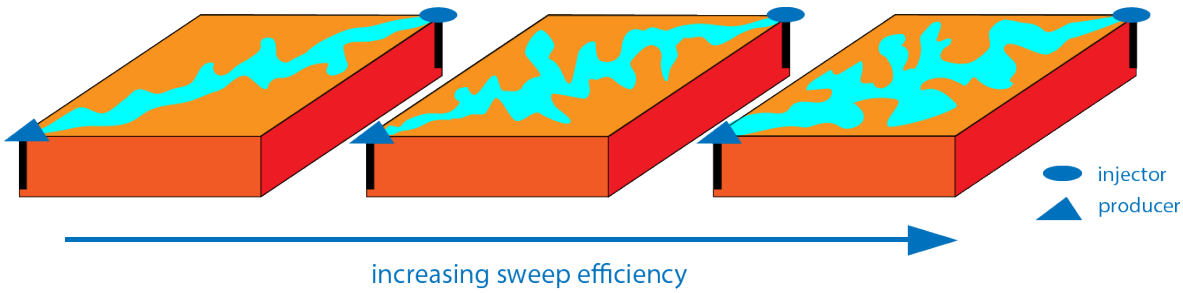


**Figure 2-8:** Diagram showing increasing areal sweep efficiency.

The same logic behind utilizing tracers for EOR sweep efficiency estimates may be applied to heat recovery for geothermal applications. Tracers can additionally be used during carbon storage to understand how the $CO_2$ is migrating throughout the reservoir. By using different tracers for each injector, all injector-producer pair communications can be mapped out in a reservoir. Recovery of a tracer in a production well from a known injection well proves connectivity between those two wells.

> ***"Detection of a tracer in a producer proves communication from the relevant injector and that producer. By tracking all injectors with different tracers, all injector-producer communications can be mapped out in the reservoir."*** - Olaf Huseby (Resman Energy Technology, 2022)

Not only can the communication between wells be determined, but the significance of the communications can be determined as well. How much tracer from each injection well is being recovered? Failure to recover a significant amount of tracer might point to potential leakage. Tracer campaigns can substantiate geophysical measurements to identify leakage pathways (Myers et al., 2013).

Below we summarize the tracer applications discussed above. Tracers, notably in the context of $CO_2$ Plume Geothermal, may be used for determination of . . .

- directional flow trends & connectivity
- volumetric sweep efficiency
- leakage pathways

For our purposes, we want to determine the volumetric sweep efficiency for $CO_2$ Plume Geothermal (CPG). Once the objectives of a tracer study are clear, it is then important to understand the value a tracer campaign can bring to a project. We want to determine, does the information gained from a tracer test outweigh the cost required to design and implement such a test? This concept can be referred to as the Value of Information (VOI). The VOI can be defined as the difference between the value of the project with the information ($VP_{\text{with info}}$) and its value without the information ($VP_{\text{without info}}$) (Bratvold et al., 2007) as demonstrated in Equation 2-3.

$$VOI = VP_{\text{with info}} - VP_{\text{without info}} \tag{2-3}$$

Thus, for a tracer test to provide valuable insights, the VOI must be non-negative and non-zero ($VOI > 0$), such that

$$VP_{\text{with info}} > VP_{\text{without info}} \tag{2-4}$$

The VOI derived from seismic surveys, wireline-logging, coring, and reservoir modelling are commonly considered for upstream oil and gas purposes (Bratvold et al., 2007) and the same surveillance and monitoring techniques may be conducted for CPG. While the cost of

undertaking a tracer test pales in comparison to construction of a commercial CPG plant, it is still important to consider the value of this information and if it can even provide useful information. This study aims to determine if a tracer field campaign provides value and is effective in enhancing sweep efficiency estimates and de-risking commercial CPG. To do this, we must now determine which tracer to use.

### 2-2-3 Tracer Types

A variety of tracers exist for different applications. We previously discussed the behavior of different tracers, but choosing the type of tracer is very important depending on what is being investigated.

Heat as a non-conservative tracer can be used to determine flow patterns in groundwater, surface water infiltration, and recharge/discharge rates for near-surface groundwater studies (Anderson, 2005). Stable Hydrogen and Oxygen isotopes can be used to differentiate between rainwater, surface water, and groundwater to determine the meteoric water line also for groundwater studies (Goni, 2006). Dye tracers are commonly used to prove connectivity and to determine flow rates more accurately than heat, but the strong sorbtive tendencies of dye lead to lower mass recovery (Leinbundgut and Seibert J, 2011), therefore their application is limited to reservoirs with short residence times such as in karst settings (Wagner, 1977). DNA-Labled Silica Nanotracers can be used for tomographic reservoir imaging using conductivity values in the shallow subsurface and potentially for other applications as a particulate tracer. These DNA nanotracers can encode information allowing for almost an infinite number of distinct tracers. Additionally they have a layer of protection from the silica coating, relatively high mass recovery rates, and little dispersion. However, these nanotracers also have strong sorbitive tendencies (Kong et al., 2018). Radioactive tracers such as tritiated $CH_4$ were used in the oil and gas industry to determine volumetric sweep efficiency of EOR, but this ceased due to environmental and health safety concerns (Myers et al., 2013).

We can see in Table 2-1 that liquid and gas chemical tracers are better suited when wanting to prevent chemical reactions or absorption in the reservoir such as for carbon storage. Additionally, gas and chemical tracers are detectable at low limits especially if they are not already present in the reservoir. This allows for more accurate recovery results during tracer campaigns. Thus, liquid and gas tracers are better suited for carbon storage, and as we want a substance to dissolve in gaseous $CO_2$, gas tracers are optimal for this study.

### 2-2-4 Gas Tracers

Gas tracers have been used in atmospheric and oceanic studies and can be used for tracking groundwater (Ren et al., 2023). As early as 1946, a helium tracer was used during gas injection, however, background concentrations of helium are too high to detect artificially injected amounts with accuracy (Frost, 1946). Most of the noble gases share this issue even though their chemical inertness makes them attractive to use as a tracer. Heightened natural occurrence of helium may be used at the surface in some cases to detect blind geothermal systems (Frost, 1946). Sulfur hexafluoride (SF6) is a commonly used gas tracer for subsurface studies. It is non-toxic, inexpensive, present at low background concentrations, has a low detection limit, inert and safe [59] (Ren et al., 2023). However, SF6 is only one unique tracer,

**Table 2-1:** Properties of Different Tracers

| | DNA nanotracers | Dyes | Liquid/Gas chemical tracers |
|---|---|---|---|
| Inert and Stable | conditional | no | yes |
| Passively follows the correct phase and is non-absorbing | no | no | yes |
| Neither present in or masked by the reservoir fluid | yes | yes | yes |
| Does not affect the physical properties of the reservoir fluid | yes | yes | yes |
| Detectable at low concentrations | conditional | no | yes |

Here we see a comparison between the properties of DNA nanotracers, dye tracers, and liquid/gas chemical tracers.

therefore it would not be possible to identify or tag multiple injection wells with different tracers. Additionally, in carbon storage isotopically distinct $CO_2$ would provide the best mimic of the injected fluid, behaving passively (Myers et al., 2013) despite the large changes in volume with an increase in temperature, pressure, and depth as seen in Figure 2-2. In this study, ideal $CO_2$ tracers are used for reservoir simulations. These serve as a proxy for the tracer field campaign which will utilize perfluorocarbon tracers (PFTs) (Leinbundgut and Seibert J, 2011).

### 2-2-5 Perfluorocarbon Tracers

PFT are highly stable, conservative, chemically inert, inexpensive, and detectable at even lower limits than SF6. The most common PFTs are perfluoromethylcyclopentane (PMCP), perfluorodimethylcyclobutane (PDMCB), perfluoromethylcyclohexane (PMCH), but there exists a wide range of commercially available cyclic PFTs (Myers et al., 2013). Their properties can be seen in Figure 2-9. Since so many PFTs exist, several may be used in the same study. In this way, the $CO_2$ from a specific injection well may be "labelled" with a single PFT. These labels may be identified and differentiated within a given sample at a production well (Leinbundgut and Seibert J, 2011). While PFTs do not completely replicate the behavior of $CO_2$ in all phases, they are ideal and will serve as the best tracer for the purpose of field campaigns for CPG.

### 2-2-6 Tagged $CO_2$ Tracers in CMG

Tracer components were made using the same component properties of $CO_2$ in CMG reservoir modelling software. Tagged $CO_2$ ($CO_2$-1 – $CO_2$-10) were injected at various intervals for the purpose of this study. Within our inverted 5-spot well-pattern there is only one injection well, so tagged $CO_2$ provides information on $CO_2$ plume development and volumetric sweep efficiency over time. A mass of 2809170 kg of each tracer was injected over 24 hours in CMG reservoir simulation software, however this amount is not realistic in the field. A mass of 5

**TABLE 6.6—PROPERTIES OF THE MOST FREQUENTLY APPLIED PERFLUOROCARBON GAS TRACERS (after Dugstad[11])**

| Perfluorocarbons Tracer | Abbreviation | Chemical Formula | Molecular Weight | Boiling Point |
|---|---|---|---|---|
| Perfluoromethylecyclopentane | PMCP | $C_6F_{12}$ | 300 | 48 |
| Perfluorodimethylcyclobutane | PDMCB | $C_6F_{12}$ | 300 | 45 |
| Perfluoromethylecyclohexane | PMCH | $C_7F_{14}$ | 350 | 76 |
| 1,3 Perfluorodimethylcyclohexane | 1,3-PDMCH | $C_8F_{16}$ | 400 | 102 |

**Figure 2-9:** Properties of perfluorocarbon gas tracers (Dugstad, 1992).

kg should be injected in a field setting, as discussed below. Injection duration, consequently, will be shorter (5 - 6 hours). This is also discussed below.

## 2-2-7 Measurements in the Field

Two types of tracer tests may be employed in the field: inter-well tracer tests IWTT and single-well tracer tests SWTT. IWTT utilize the connectivity between an injector-producer well pair, whereas SWTT utilizes only one well for the purpose of determining the remaining oil saturation near the well bore (Patidar et al., 2022). For our purposes, an IWTT is used as we would like to investigate the volumetric sweep efficiency in our reservoir.

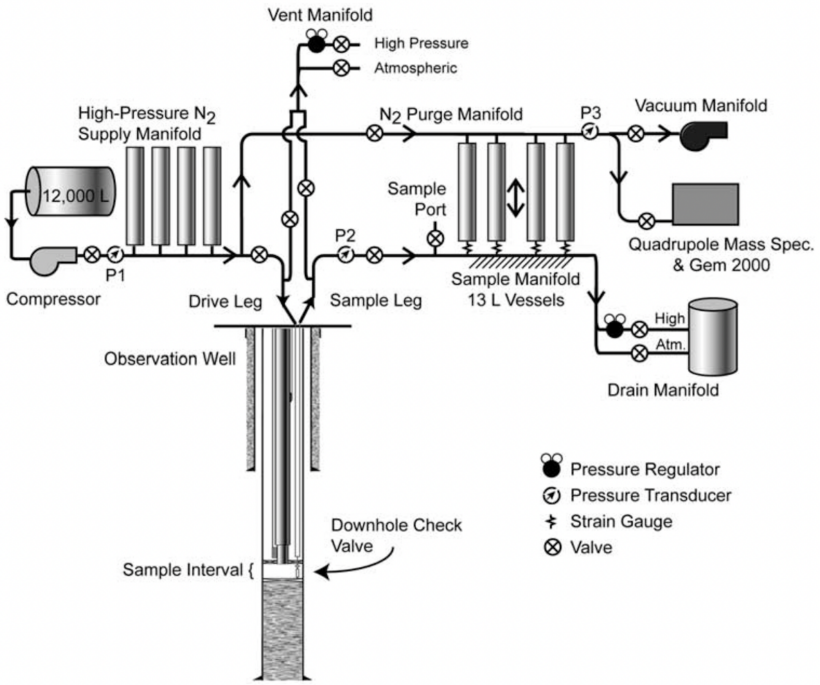


**Figure 2-10:** Simplified diagram of the U-tube sampling system (Freifeld et al., 2005)

A gas chromatograph, also called a mass spectrometer, may be used for detection of the tracer at the production well. Continuous monitoring must begin upon injection of the tracer. By sampling before the tracer arrives at the production well, a background concentration is established of chemicals in the fluid. The Agilent 6890N gas chromatograph has previously been used for perfluorocarbon gas tracer studies in carbon storage projects (Blaushild, 2015) and can sample at various intervals. Novel down-hole sampling device, U-tube, for PFT in multi-phase fluid in carbon sequestration projects utilizes a quadrupole mass spectrometer for real-time gas analysis (Lu et al., 2012; Freifeld et al., 2005; Soltanian et al., 2018). Above we see a diagram of this instrument placed in an observation well. For our purposes, we are interested in measuring PFT tracers from fluids at the production well. However, components from this sampling system may be implemented at a production well. A pressure regulator connected by valves to the gas chromatograph is necessary to lower the pressure of the sample taken from the well. Valves are computer-controlled to allow for the automation of sampling. An additional sample port allows for samples to be collected for lab analysis and comparison with field measurements.

Regarding injection quantity, it is not necessary for a large quantity of the tracer to be injected due to the low detection limits of PFTs. PFT have a detection limit of 200 femtoliter or parts per quadrillion (Blaushild, 2015). Soltanian et al. injected 5.2 kg of PFT over two hours. Freifeld et al. injected 3 kg of PFT over five hours. McCallum et al. injected 4 kg of PFT over five hours. Therefore, a recommendation of 5 kg PFT injected over 5 - 6 hours is made for a well spacing of 1 km, such as is the case used in this study.

### 2-2-8 Tracer Recovery Interpretation

Traditionally, Shook's method (Shook and Forsmann, 2005) may be employed for calculating the first temporal moment and the swept volume of the reservoir. However, this method assumes a constant density. Water-based tracers are incompressible, and thus maintain a constant density. We can see the assumption of a constant density for calculating the age distribution function, $E(t)$, for incompressible fluids in Shook's method below and also in Appendix A.

$$E(t) = \frac{C(t) * \rho * q_{inj}}{M_{inj}} \tag{2-5}$$

where $E(t)$ has units $\frac{1}{day}$, $C(t)$ is the produced tracer concentration $(ppb)$, $\rho$ is the density $(kg/m^3)$, $q_{inj}$ is the volumetric mass injection rate $(\frac{m^3}{day})$ and $M_{inj}$ is the mass of the injected tracer $(kg)$.

However, supercritical $CO_2$ is a compressible fluid, resulting in highly variable density, depending on temperature, pressure, and depth conditions. This was previously visualized in Figure 2-2. Thus, Shook's method cannot be utilized in our case. However, it could be useful to do a water tracer analysis as a pre-flush and compare the results with those from the $CO_2$ tracers. A brief description of Shook's analysis can be found in Appendix A.

Qualitatively, we may make same interpretations of tracer recovery curves. We see in Figure 2-11 some examples. In Figure 2-11a transport processes such as advection, dispersion, sorption, and decay are visualized. Dispersion leads to Gaussian recovery of a tracer signal. Sorption

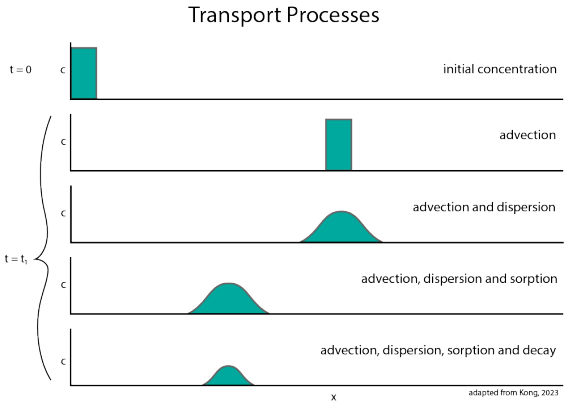


**(a)** Transport processes that impact tracer recovery

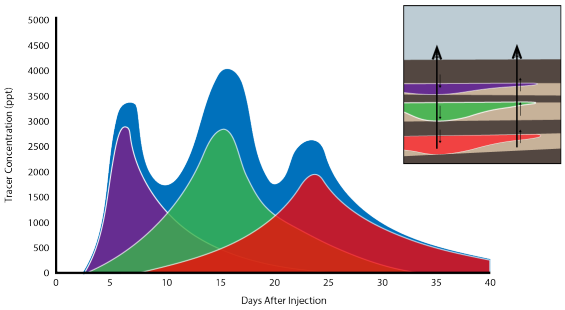


**(b)** Example tracer recovery curve (blue) with corresponding tracer slugs (purple, green, red)

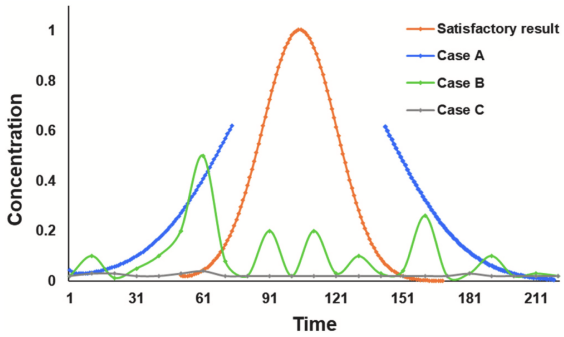


**(c)** Unsatisfactory tracer recovery (Ren et al., 2023)

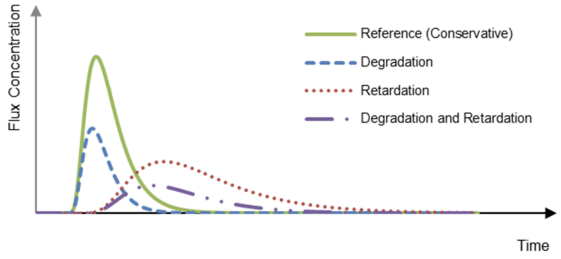


**(d)** Conservative vs. Reactive tracers (Cao et al., 2020)

**Figure 2-11:** Tracer recovery examples

leads to quicker recovery of a tracer due to adherence on the rock. Decay in the case of non-conservative tracers such as heat leads to smaller mass-recovery. In Figure 2-11b an explanation is given for potential multi-modal breakthrough curves. The partitioning of a tracer into multiple layers might cause the mixing of tracer slugs. Individual slugs may be partitioned through deconvolution using Shook's method described in Appendix A.

In Figure 2-11c unsatisfactory tracer recovery is compared against a satisfactory result. Unsatisfactory Case A might occur due to insufficient collection duration. Case B might occur due to well leakage and flow through multiple permeable layers. Case C might occur due to insufficient tracer mass injected (Ren et al., 2023). Additionally, there could be a loss of fluid injected, leading to low mass recovery. Fluid loss, according to Patidar et al. may be attributed to any of the following factors:

- existence of fractures/faults where fluids might escape through
- poor sampling, resulting in inaccurate recovery values
- presence of an unknown aquifer that might dilute the tracer concentrations to below the detection limit

In Figure 2-11d a comparison between conservative and reactive tracers is given (Cao et al., 2020). The effects of degradation and retardation are shown. These examples can inform our own interpretation of breakthrough curves for this study.

### 2-2-9 Volumetric sweep efficiency determination

Volumetric sweep efficiency may then be calculated using the following equation provided by Kantzas et al.. Notably, the area of displacement and gas saturation must be known for this determination of sweep.

$$E_V = E_{AS} * E_{VS} = \frac{A_d}{A_R} * h * \phi * S \tag{2-6}$$

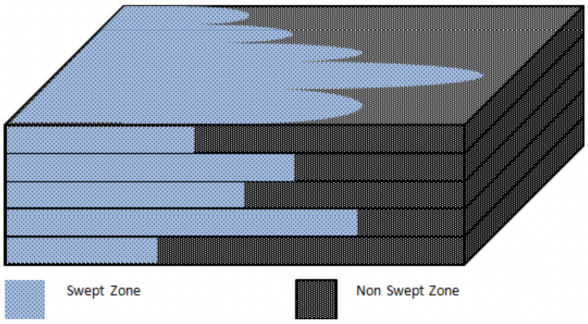


**Figure 2-12:** Example of volumetric sweep in a stratified reservoir (Kantzas et al., 2023)

where $E_{AS}$ is areal sweep efficiency, $E_{VS}$ is the vertical sweep efficiency, $A_d$ is area of displacement, $A_R$ is area of the reservoir, $h$ is the height of the reservoir, $\phi$ is porosity, and $S$ represents gas saturation. This is visualized below in a stratified reservoir. Heterogeneity and mobility of our fluid greatly impact sweep efficiency.

The temporal moment or mean residence time ($m_k$) may be calculated as follows, where $t$ is time and $c$ is concentration of the $k$th breakthrough curve.

$$m_k = \int_0^\infty t^k c(x,t)\, dt \tag{2-7}$$

Chapter 3

# Methods

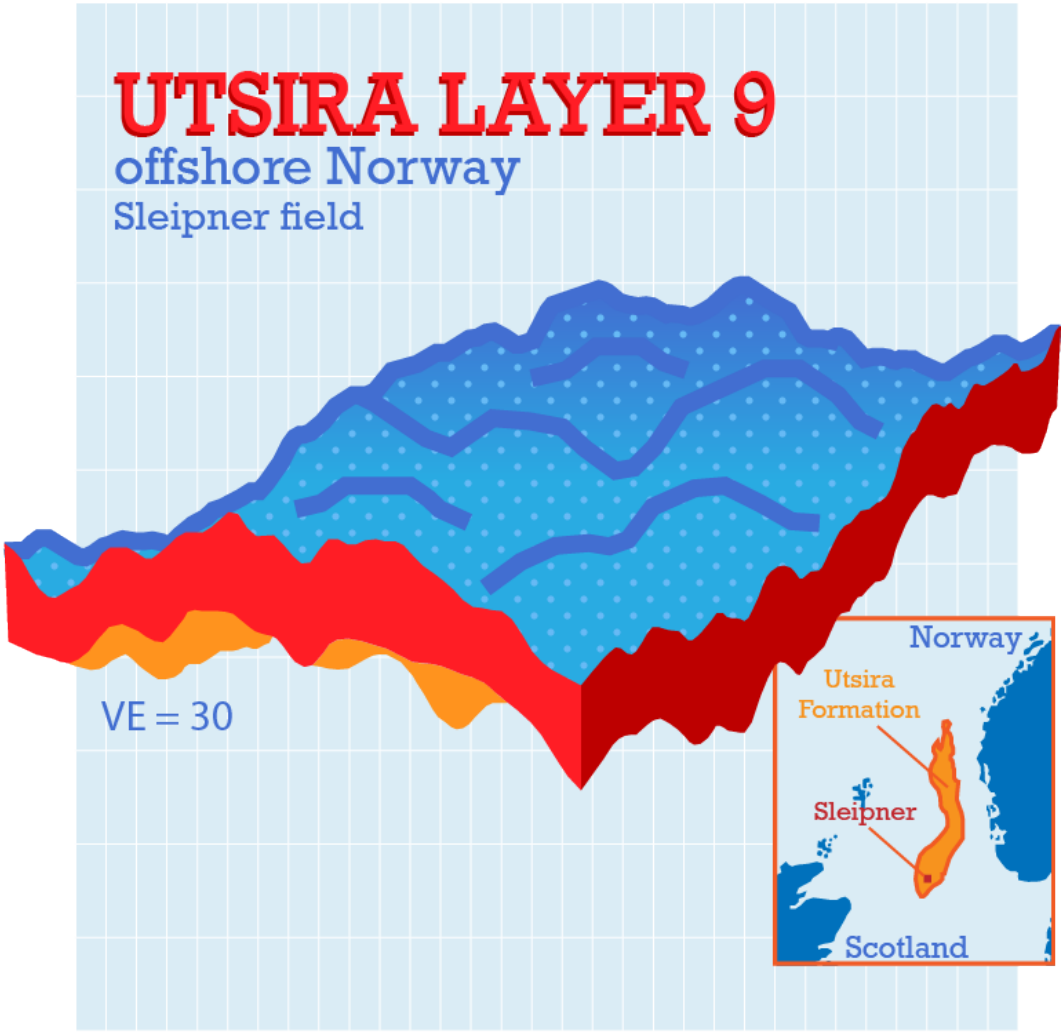

# 3-1 Data

## 3-1-1 Sleipner Field

The North Sea is an important area for oil and gas production and, now, carbon storage. With an estimated storage capacity of 160 gigatons, the North Sea can store 75 years' worth of Europe's present $CO_2$ emissions (Equinor, 2020). Northern Lights, a full-scale CCS project operated by Equinor, Shell, and TotalEnergies is set to utilize this massive storage capability in a large way starting 2024 (Equinor ASA, 2023). However, the Sleipner project was the first CCS project in the North Sea.

The Sleipner Carbon Storage Project located 250 km off the coast of Norway was the first offshore CCS project ever (Equinor, 2020). Additionally, it was the first subsurface $CO_2$ project in Europe and the first commercial-scale project for carbon storage in a saline aquifer (Equinor, 2020), (Metz et al., 2005).

## 3-1-2 History of CCS at Sleipner

In 1996, CCS began at the Sleipner field, operated by Statoil, now Equinor. Injecting approximately 1 million tons of $CO_2$ per year through one injection well, Equinor has safely stored more than 20 million tons of $CO_2$ since 1996 (Equinor, 2020). This $CO_2$ originates from the hydrocarbon processing emissions of gas from nearby fields Sleipner Øst, Gungne and Sleipner Vest. During processing of the natural gas, 9% $CO_2$ is present. However, in order to meet export and consumer requirements, the gas must contain maximum 2.5% $CO_2$. If the excess $CO_2$ were to be released into the atmosphere, then gas field operators would need to pay hefty fines according to the 1991 Norwegian $CO_2$ tax (MIT, 2015). Thus, Statoil created the CCS unit to safely store their excess $CO_2$. Since the advent of their carbon storage operations, Statoil has partnered with the International Energy Agency Greenhouse Gas R&D program in the Saline Aquifer $CO_2$ Storage (SACS) program to conduct research and monitor CCS activities (Metz et al., 2005).

## 3-1-3 Research and Monitoring Activities

After over 25 years of $CO_2$ injection and monitoring, extensive research has been done on the Sleipner field (Alnes et al., 2011; Hermanrud et al., 2009; Zweigel et al., 2000; Akervoll et al., 2009). Equinor has undertaken multiple monitoring initiatives to guarantee the long-term storage of $CO_2$. Bottomhole pressure is monitored to ensure steady injection rates and to prevent induced seismicity. 4D seismic has tracked the propagation and fluid pathways of $CO_2$ in order to identify leakage pathways. An example of such seismic monitoring and later modelling of $CO_2$ accumulation and migration pathways is seen in Figure 3-1. In order for a basin to serve as a secure storage reservoir, it must meet the criteria listed in subsection 1-2-2. The Sleipner field meets all of these criteria and potential leakage is continuously monitored. Upon the closure of the Sleipner field, monitoring operations will continue for at least 20 years as mandated by the European Parliament and the Council of the European Union (European Parliament, 2009).

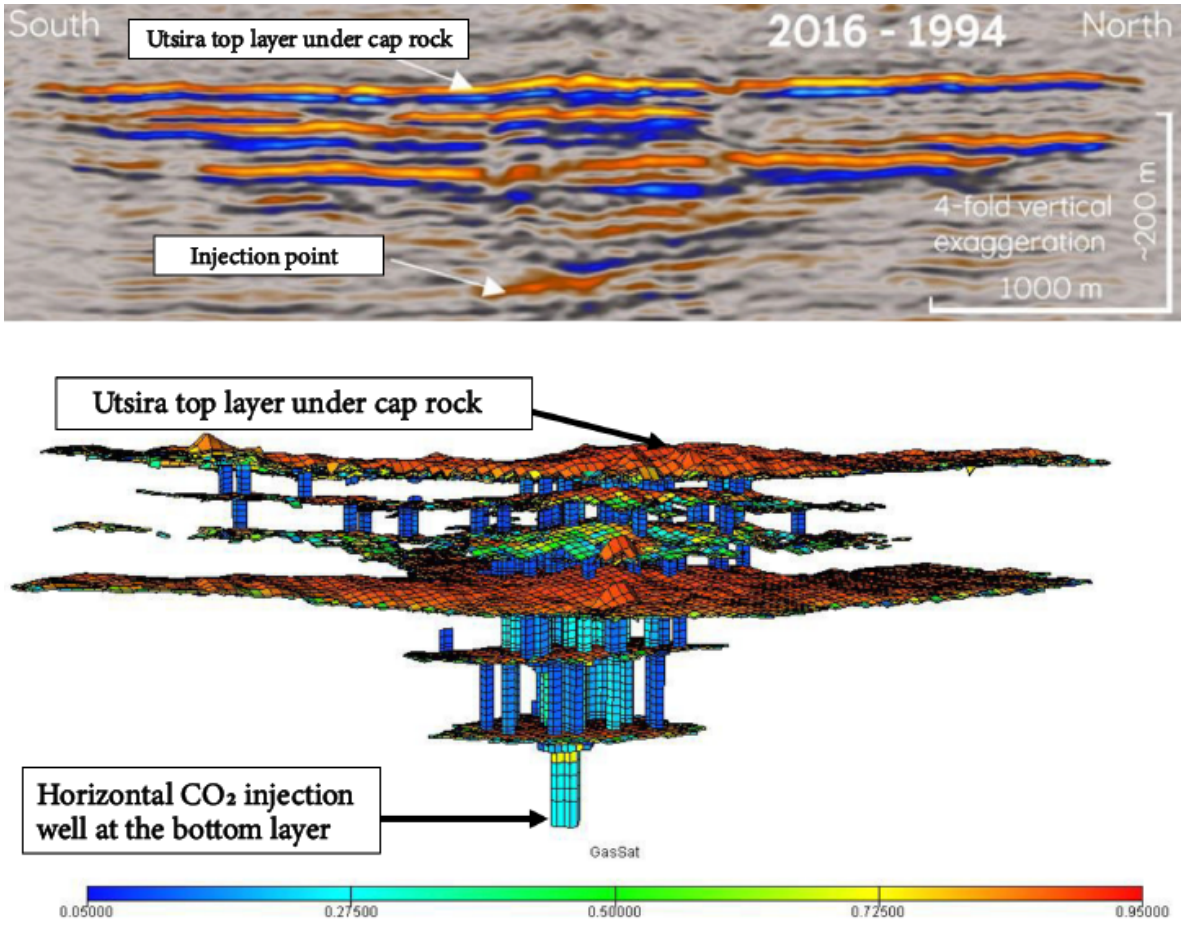


**Figure 3-1:** Time lapse seismic data of $CO_2$ injection from 1994 to 2016 (top) (Equinor, 2020) and pathways from modelling (bottom) (Akervoll et al., 2009) in the Utsira formation of the Sleipner field in offshore Norway. The vibrant yellow and blue colors in the top image represent $CO_2$ accumulation beneath a shale caprock and between thin shale layers (Equinor, 2020). The presence of a leak through the caprock would be visible in such a seismic section.

Additionally, as of 2016 Equinor together with the IEA has made some of their data publicly accessible via the $CO_2$ Storage Data Consortium. The goal of the consortium is to promote knowledge exchange and with larger goals to improve understanding, reduce costs, and minimize uncertainties associated with $CO_2$ storage (International Energy Agency (IEA), 2023). SINTEF, the University of Illinois, Gassnova, and the US Department of Energy have joined them in their efforts. This study utilizes the Sleipner $CO_2$ reference dataset published via the $CO_2$ DataShare online portal administered by Stiftelsen for Industriell og Teknisk Forskning (SINTEF).

Below, SINTEF describes the details of the data license,

> *"Subject to... Terms and Conditions, The Sleipner Group grants you a worldwide, royalty-free, non-sublicensable, non-exclusive, irrevocable license to download and use the Licensed Material for non-commercial and commercial purposes, including to create, produce and reproduce Adapted Material"* - Sleipner $CO_2$ Reference Dataset License (SINTEF, 2019)

### 3-1-4 Geology

The Sleipner field consists of nine sandstone layers, Utsira L1 - L9, separated by thin shale layers and covered by a thick shale caprock. The Utsira formation is a Miocene shallow marine sandstone formation that overlies the Jurassic oil/gas-bearing formations that are targeted at greater depth. The Utsira has a depth of 800 – 1000 meters below the seabed of the North Sea. Interbedded shale layers are fairly thin ( 1 m), except for the shale layer between L8 and L9 ( 7 m), referred to as the "Thick Shale Unit ". The influence of thin laterally-discontinuous shale beds on $CO_2$ migration is visualized in Figure 3-2. The caprock is represented in the full model by a 50 m thick shale unit, but the actual formation is much thicker (CO2DataShare/CSDC and Equinor, 2020).

Only a portion of the Sleipner field will be used here as the full model requires significant computational power and a single sandstone layer is suitable for our purposes. Therefore the Utsira Layer 9, or the top sandstone layer, will be investigated in this study.

### 3-1-5 Dataset

In the $CO_2$ Data Share portal, a range of information from well data to velocity maps exist. For more information on all provided data, the reader is directed to (CO2DataShare/CSDC and Equinor, 2020) directly. Here, we make use of the Sleipner Reference Model 2019 Grid provided by SINTEF within the portal. The full grid consists of a 3D simulation grid in RESCUE file format with approximately 2 million cells (64 x 118 x 263) Figure 3-3. The model spans 3.2 km by 5.9 km with a thickness

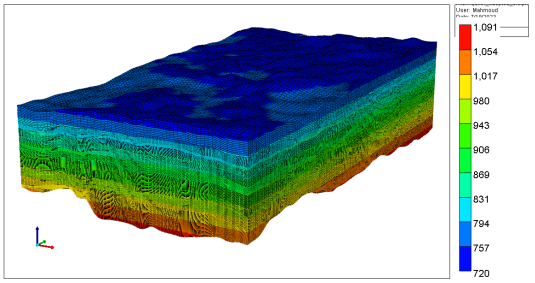


**Figure 3-3:** Sleipner model

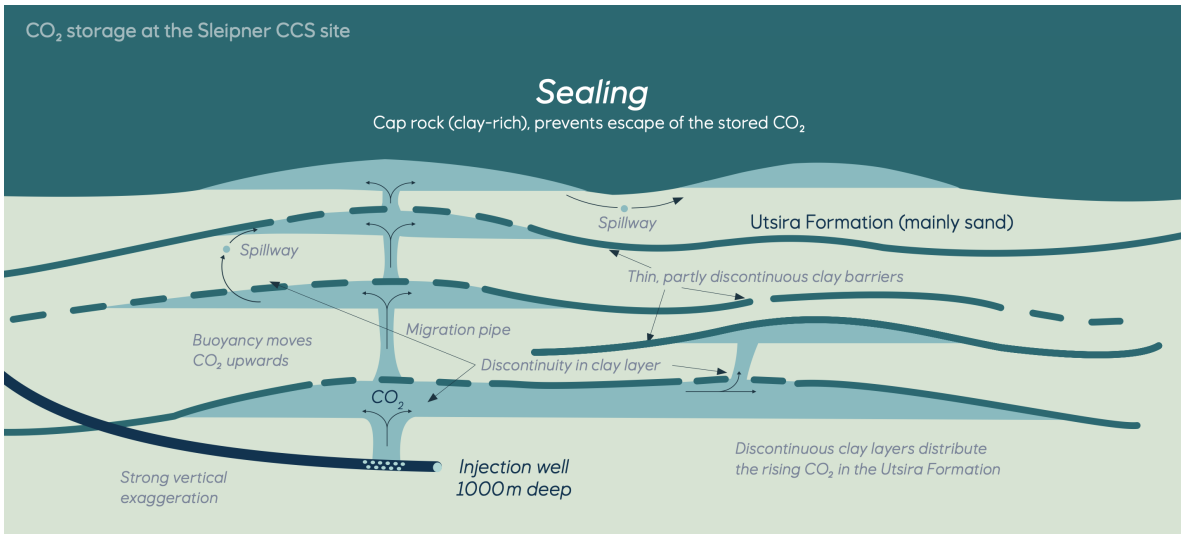


**Figure 3-2:** $CO_2$ fluid pathways in the Utsira formation of the Sleipner field. Discontinuous clay layers allow $CO_2$ to rise toward upper layers of the Utsira formation which consists of nine sandstone layers (Equinor, 2020).

of up to 300 m. Properties are resolved laterally in 50 m by 50 m grid cells and vertically by ∼2 m. However, properties within the intrashale and caprock cells are resolved in 0.5 m and 5 m intervals, respectively.

For the Utsira Layer 9 specifically, there are 120,832 active grid cells (64 x 118 x 16) with a maximum thickness of 77 m. In Figure 3-4 we see this top sandstone layer with a vertical exaggeration of 30. There are gentle anticlinal structures that provide the structural trapping mechanism for $CO_2$.

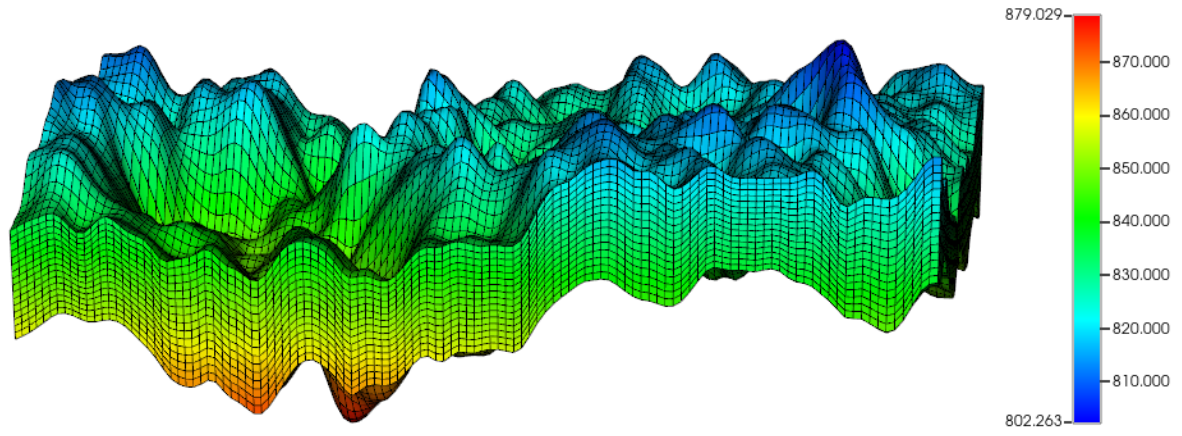


**Figure 3-4:** Utsira Layer 9, depth in meters (120,832 active grid cells)

The below porosity Figure 3-5a and permeability models Figure 3-5b are for the whole field. Here we see that uniform porosity and permeability is imposed within the individual

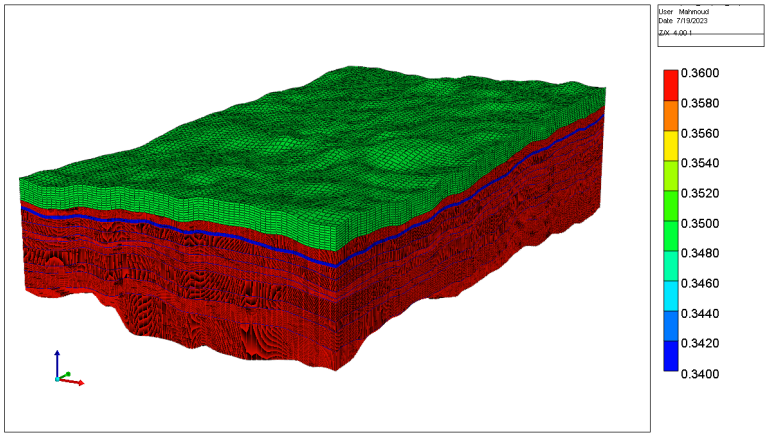


**(a)** Sleipner field porosity model

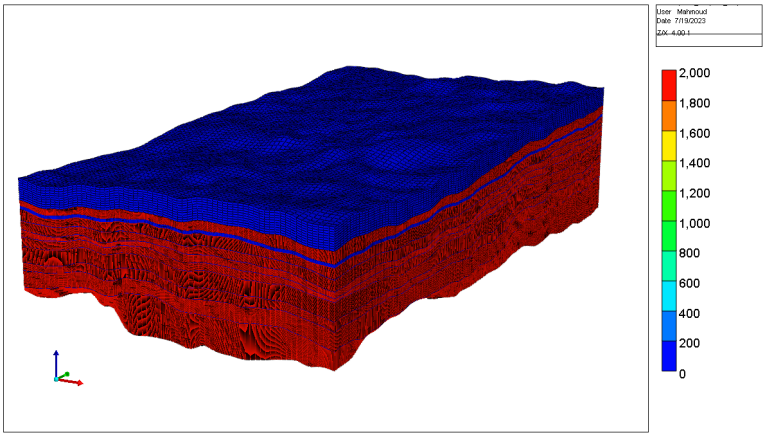


**(b)** Sleipner field permeability model

lithologies for an isotropic model. The caprock, Utsira sandstone formations, and interbedded shales have porosity values of 35, 36, and 34, respectively. Corresponding permeabilities are 0.001, 2000, and 0.001, respectively. However, some uncertainty exists for the estimates of porosity and permeability due to variable clay content and effective stress. Focusing on the Utsira Layer 9, we continue to assume a porosity of 36 and a permeability of 2000 mD. These values are listed in Table 3-1 and are taken from (Lothe and Zweigel, 1999; Zweigel et al., 2000; Holloway et al., 2000; Lindeberg and Holt, 2000).

However, a range of permeability values is suggested by (Lindeberg and Holt, 2000). Therefore, some heterogeneity is imposed on our model to represent a range of potential heterogeneity as uncertainty exists. Imposing heterogeneity may be performed in different ways. However, we chose to implement a stratified method in our heterogeneous models, assuming permeability decreases with depth. Such a stratified model was previously discussed in subsection 2-2-9. We see in Figure 3-6, Model 1 has a permeability range of 2750 - 1250 mD, Model 2 has a range of 2500 - 1500 mD, and Model 3 has a constant permeability of 2000 mD. By imposing isotropic conditions in the xy-direction, $CO_2$ migrates uniformly and radially

**Table 3-1:** Utsira porosity and permeability values

| Model Parameters | Symbol | Unit | Reference Value | Range | References |
|---|---|---|---|---|---|
| Utsira porosity | $\phi_{fmn}$ | % | 36 | 27-40 | Lothe and Zweigel (1999); Holloway et al. (2000) |
| Utsira permeability | k$k_{xy}$ | mD | 2000 | 1100 - 5000 | Lindeberg and Holt (2000) |

Porosity and permeability values, value ranges, and data source for the Utsira formation to inform the static reservoir model.

in the xy-direction, affected only by topography in the model. However, in the z-direction, we impose anisotropy resulting in variable mobility in different layers within the reservoir. Three versions Model 1, Model 2 and Model 3 will be tested to see how heterogeneity impacts sweep. Below we see the three models that are implemented in our study.

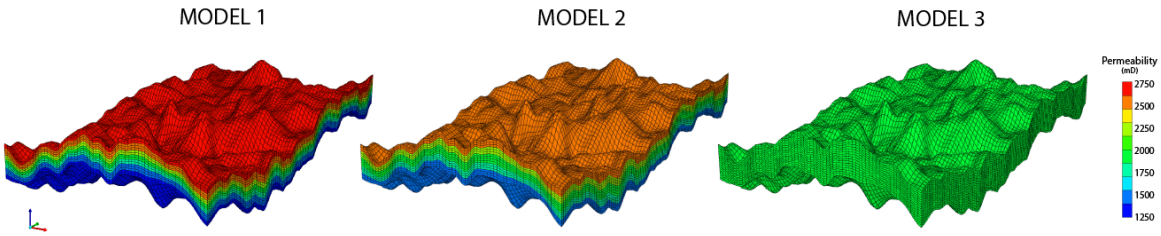


**Figure 3-6:** Heterogeneous models: Model 1, Model 2, Model 3. Model 1 has a permeability range of 2750 - 1250 mD, Model 2 has a range of 2500 - 1500 mD, and Model 3 has a constant permeability of 2000 mD.

These three versions Model 1, Model 2 and Model 3 were chosen to represent a coarsening and fining upwards sequence, in addition to a homogeneous model. These sequences exist in geologic settings and were chosen so as to introduce heterogeneity due to uncertainty within the model. Geologically, Model 1 represents a coarsening-up sequence with permeability increasing upwards. Model 2 represents a homogeneous model. Model 3 represents a fining-up sequence with permeability increasing downwards.

A no-flow boundary is assumed for the top and bottom boundaries. This represents an impermeable caprock above the sandstone layer and the thick shale layer beneath the sandstone, both of which prevent the flow of fluids. On the sides of the reservoir, however, a volume modifier was created (Figure 3-7) to introduce the assumption that the sandstone layer is very large and that we are only investigating a portion of the layer. The volume of the gridblocks of the boundary are set to 10,000, whereas the volume of the blocks of the rest of the grid remains at 1. By establishing a very large reservoir, a constant pressure boundary is created as opposed to a no-flow boundary. This also allows for fluids to be recovered from beyond the well pattern.

Other properties were necessary for the building of the model. The following properties and their sources are listed in Table 3-2. The relative permeability curves used in this study from Akervoll et al. are also seen below in Figure 3-8.

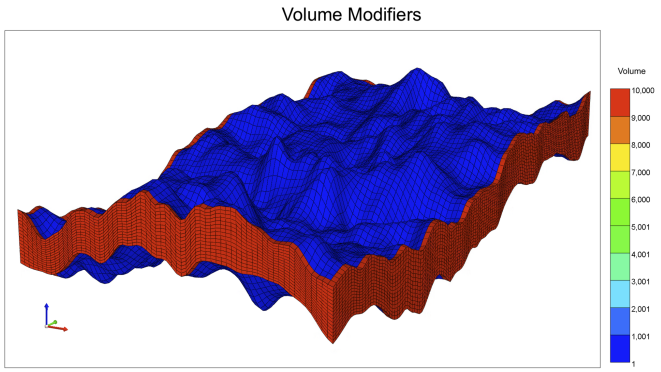


**Figure 3-7:** Volume modifier that induces a constant pressure boundary

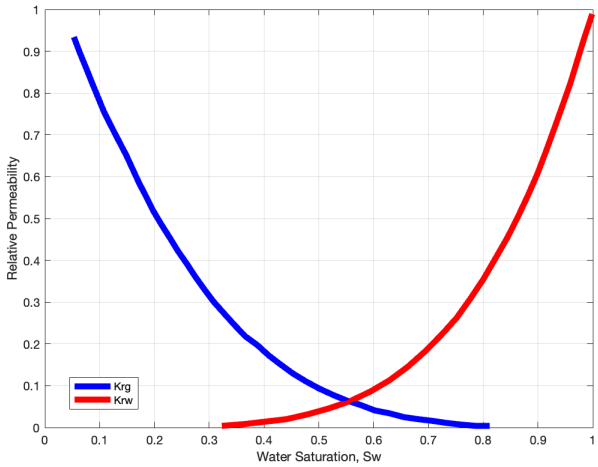


**Figure 3-8:** Relative permeability curve (Akervoll et al., 2009)

**Table 3-2:** Utsira formation rock properties

| Property | Value | Source |
|---|---|---|
| Thermal Conductivity (W/mK) | 2.4 | Nooner et al. (2007) |
| Specific Heat Capacity (J/kgK) | 1180 | Nooner et al. (2007) |
| Critical Temperature of $CO_2$ (K) | 304 | CMG Ltd. (2022) |
| Critical Pressure of $CO_2$ (atm) | 72.8 | CMG Ltd. (2022) |
| Reference Pressure at 850 m (kPa) | 8500 | Pham et al. (2013) |
| Salinity (%) | 0.035 | Lindeberg and Holt (2000) |

Temperature and pressure gradients from Alnes et al. (2011) were used to inform the temperature-depth and pressure-depth relationships for the model. Here, $z$ represents the depth in kilometers.

$$T(z) = 31.7°\text{C/km} * z + 3.4°\text{C}(\pm 0.5°\text{C}) \tag{3-1}$$

$$P(z) = 101.1 \text{ bar/km} * z + 2.4 \text{ bar}(\pm 0.2 \text{ bar}) \tag{3-2}$$

It is crucial to acknowledge that the reservoir's complexity is not fully captured in this study. Models are simplified versions of reality. The heterogeneous models and values assumed in this study may not fully reflect the variability within the reservoir or the dynamic behavior of $CO_2$ due to limited borehole data. On the basis of establishing geological models, Wellmann and Caumon write,

> ***"Unfortunately, we cannot model the entire evolution of the Earth in such a detail that we would be able to obtain a completely realistic picture of the spatial distribution of all relevant properties. Instead, we aim to formulate models that capture essential aspects of this evolution, which we deem relevant for the purpose and scale of a specific investigation."*** - Florian Wellman, Guillaume Caumon (Wellmann and Caumon, 2018)

In this study, these populated models contain some simplification but can be used to obtain information on $CO_2$ plume development to provide recommendations for a tracer field campaign.

## 3-2 Dynamic Model

We first impose an inverted 5-spot well-pattern with distance 1 km between injector and producer wells. Between producer wells there is a distance of 1.414 km. Here we see our model shaded by depth with the imposed inverted 5-spot well pattern Figure 3-9. Aerially, the grid appears as seen in Figure 3-10.

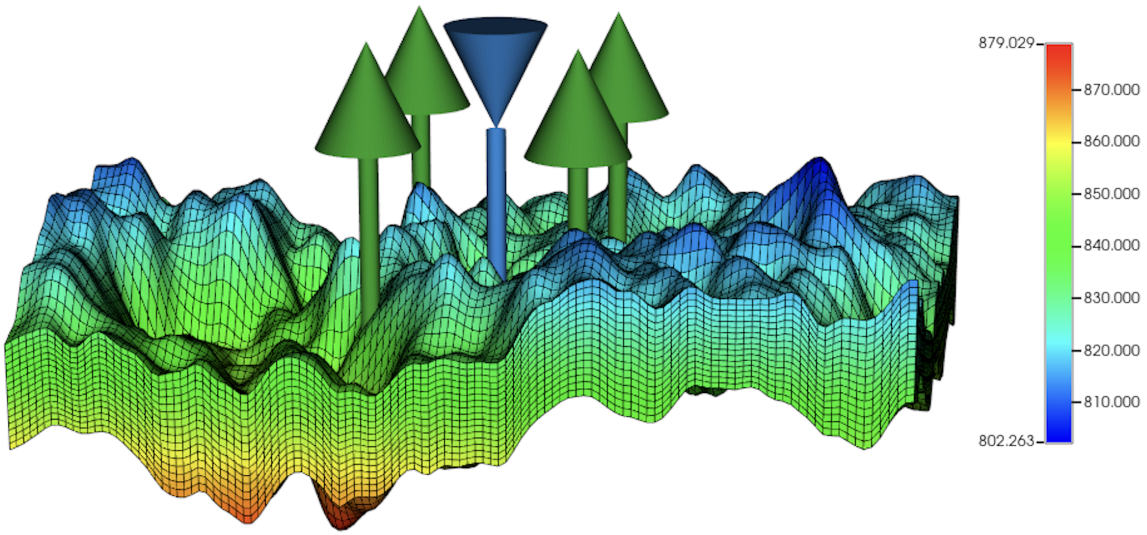


**Figure 3-9:** Utsira Layer 9 with inverted 5-spot well pattern, depth in meters (120,832 active grid cells)

The proximity of the injection and production wells can be seen in Figure 3-11. Each producer is located 1 km from the injection well in an inverted 5-spot well pattern. For similarly-scaled reservoirs, well patterns are often designed so producers are 0.7 km from the injector, however this is not the case for our well pattern. The injection well is situated on a topographic low (approx. 850 m depth at the bottom of the well) which allows the $CO_2$ to migrate upwards towards the production wells. Because the production wells were placed 1 km from the injection well, they are not located perfectly at topographic highs of the caprock base. The top of Producer 2 is situated highest in the reservoir (approx. 820 m depth), whereas Producer 3 is situated lowest (approx. 830 m depth). In these cross sections, the greatest topographic lows occur outside of the well pattern. This is especially visible in Figure 3-11d, where the reservoir reaches depths of 879 m. Therefore, the reservoir is not fully utilized, considering CPG operates best when injection wells are

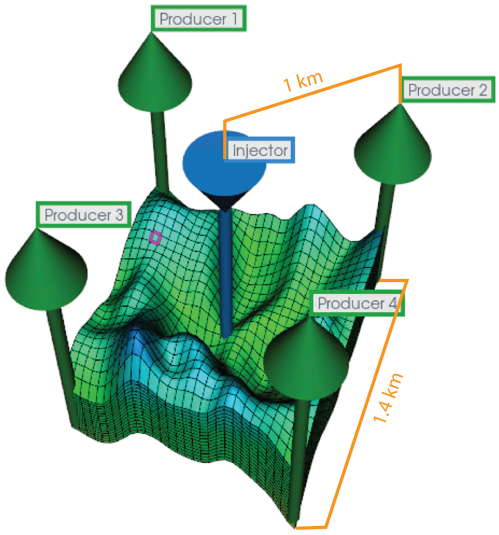


**Figure 3-10:** Aerial view of inverted 5-spot well pattern

placed significantly lower than production wells. By producing at topographic highs, more of the reservoir may be swept as the supercritical $CO_2$ heats up, expands, and rises towards the top of the well through the production well. An injection rate of $1,520,000$ m$^3$/day was assumed (Pham et al., 2013) and one-fourth of this rate is assumed for each production well, or $380,000$ m$^3$/day.

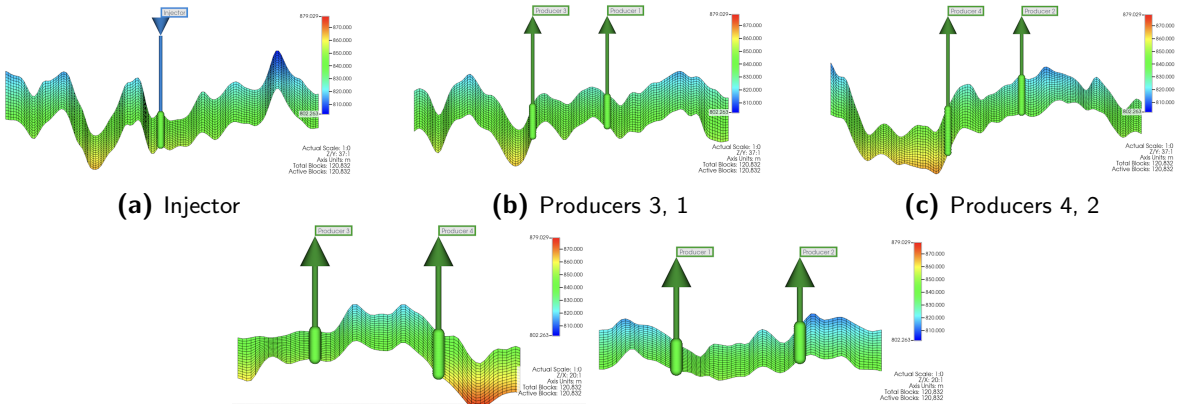

**(a)** Injector **(b)** Producers 3, 1 **(c)** Producers 4, 2

**(d)** Producers 3, 4 **(e)** Producers 1, 2

**Figure 3-11:** Well locations relative to the topography

### 3-2-1 Tracer Schedule

Four tracer schedules are investigated for the purpose of this study to determine how time between tracer injection and number of tracer injections impact tracer recovery in the three models. For this purpose four tracer injection schedules with either 3 or 7 tracers (N = 3, 7) injected in 1 or 2 month intervals (dt = 1, 2) are assumed for this study. Each tagged $CO_2$ tracer is injected for a day (24 hours). The total mass injected for each tagged $CO_2$ tracer is 2,809,170 kg at a rate of 2,809,170 kg/day.

| Schedule | Number of Tracers **N** | Injection Interval (months) **dt** | Tracers Used |
|---|---|---|---|
| 1 | 3 | 1 | CO2-1, 2, 3 |
| 2 | 3 | 2 | CO2-1, 3, 5 |
| 3 | 7 | 1 | CO2-1, 2, 3, 4, 5, 6, 7 |
| 4 | 7 | 2 | CO2-1, 3, 5, 7, 8, 9, 10 |


**Figure 3-12:** Tracer Injection Schedules with either 3 or 7 tracers (N = 3, 7) injected in 1 or 2 month intervals

# Chapter 4

# Results

## 4-1 Pressure

Upon injection, a pressure field forms (Figure 4-1). High pressure (~8000 kPa) already exists within the reservoir, and the injector induces a high-pressure zone, in which fluids are injected at a constant rate. It is most likely that gaseous $CO_2$ is present at this pressure (6000 MPa) as opposed to supercritical $CO_2$. While the production benefits of supercritical $CO_2$ are not gained from this simulation, we are still able to investigate $CO_2$ plume development, the purpose of this study.

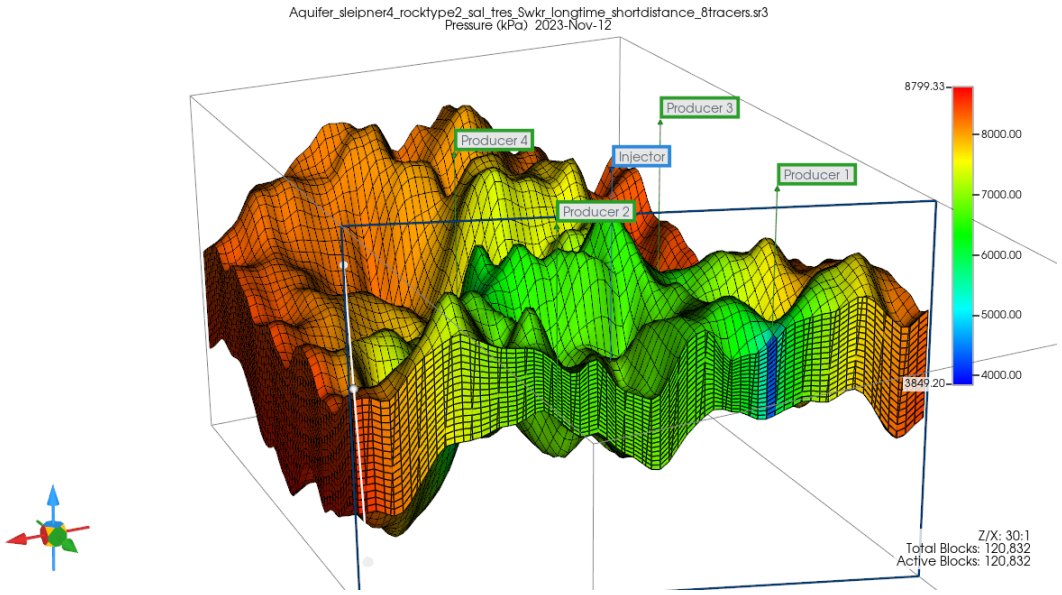


**Figure 4-1:** Pressure difference between wells. Orange/red values indicate maximum pressure of up to 8799 kPa. Dark blue values around the wells indicate minimum pressure down to 3849 kPa.

A low-pressure zone exists around Producers 1 - 4 as fluids are produced at a constant rate. This is shown in Figure 4-1 by the low-pressure zone around Producer 1 indicated by the blue color. The pressure differential within the inverted five-spot well pattern allows fluid to flow from areas of high pressure (injector) to low pressure (producers).

## 4-2 Breakthrough curves

Breakthrough curves (BTC) for all ten tagged $CO_2$ tracers for Model 1, Model 2, Model 3 and the corresponding models are seen in Figure 4-2. The curves are visualized over the course of 703 days (almost 2 years) since the start of the injection period on January 1$^{st}$, 2023.

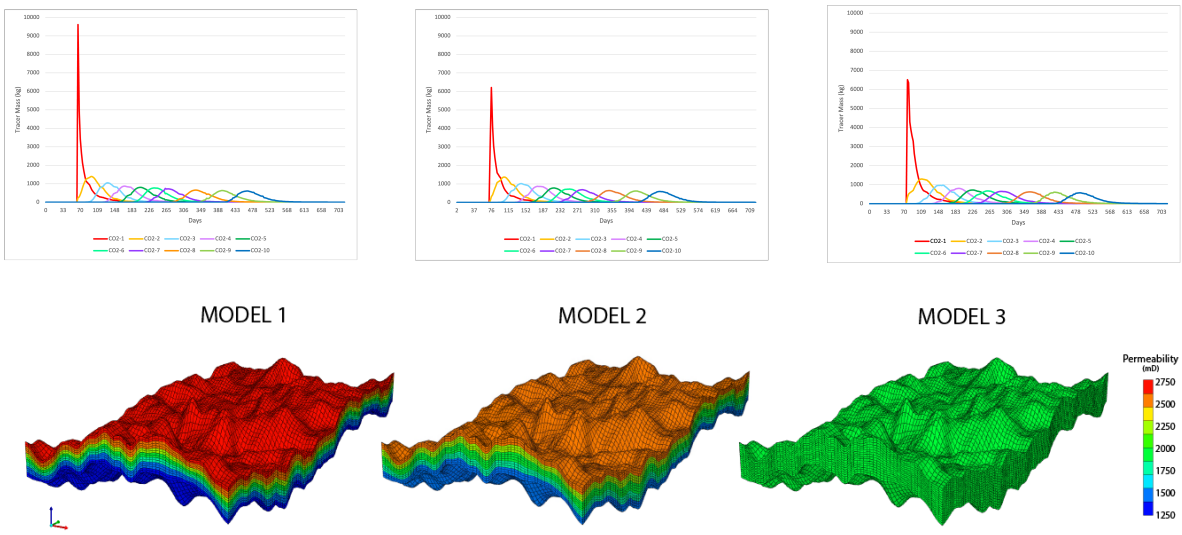


**Figure 4-2:** All tracer (N=10) breakthrough curves and the corresponding model

An example of the tracer recovery from the four tracer injection schedules plotted in days since the first injection is visualized in Figure 4-3. Model 2 is used for demonstration. Here, we see how tracer recovery evolves over time. The following results will all be plotted in days since injection of EACH pulse. This way, we may compare the recovery of the tracers against one another. On the next pages, we visualize the tracer recovery since injection for each schedule and each model, utilizing the recovery values from Producer 2 (Figure 4-4, Figure 4-5, Figure 4-6).

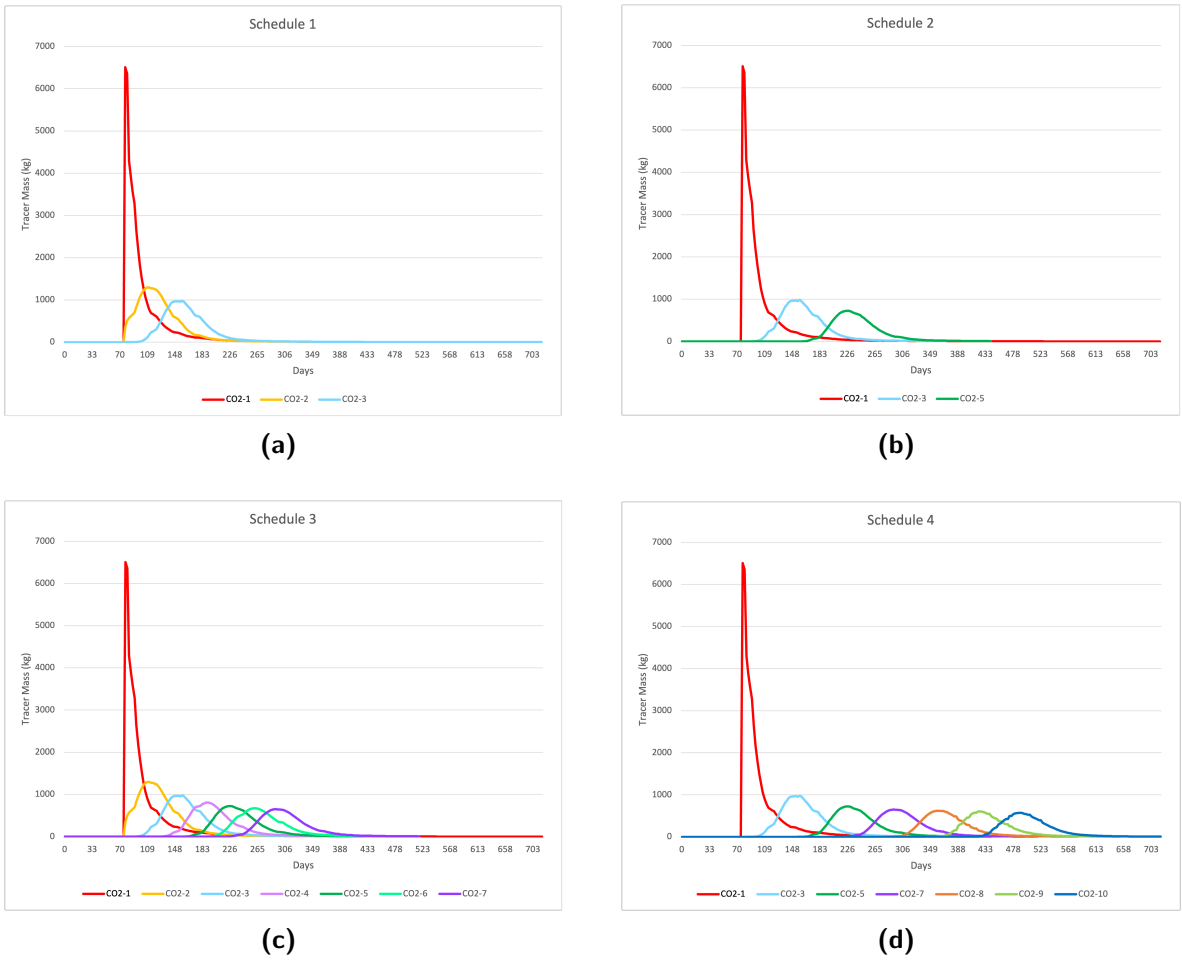


**Figure 4-3:** Tracer recovery demonstration from Schedule 1-4 using Model 3

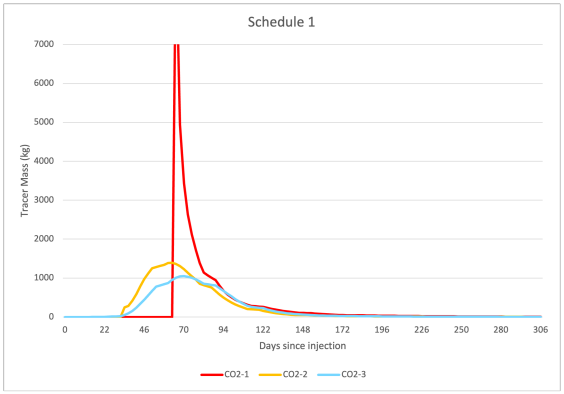


**(a)** Schedule 1

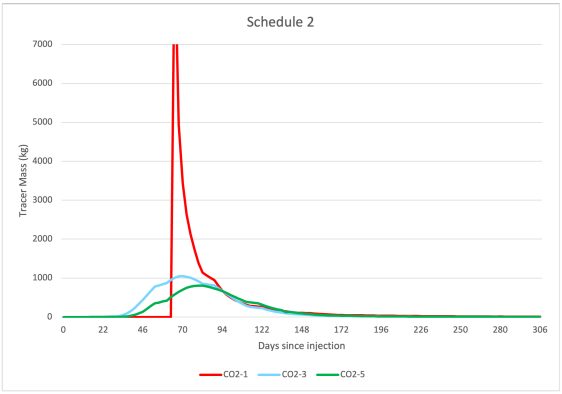


**(b)** Schedule 2

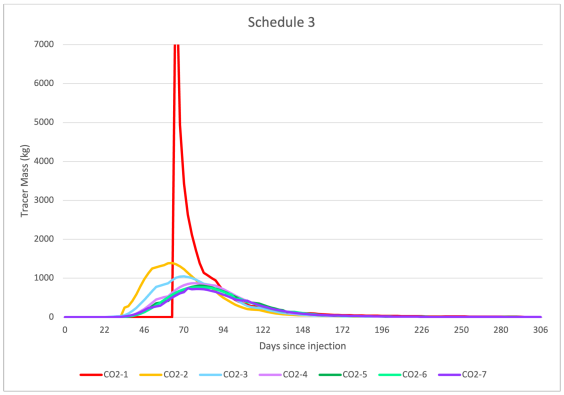


**(c)** Schedule 3

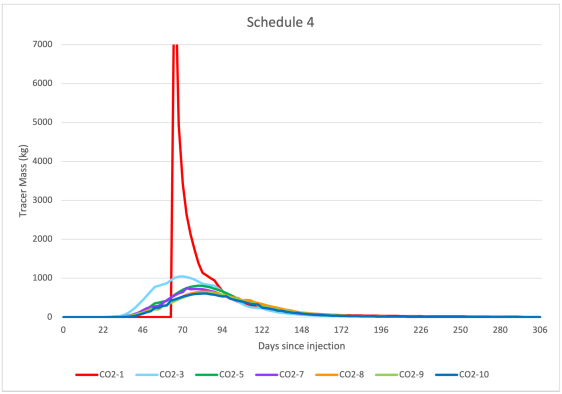


**(d)** Schedule 4

**Figure 4-4:** MODEL 1: Tracer breakthrough curves for Schedules 1-4

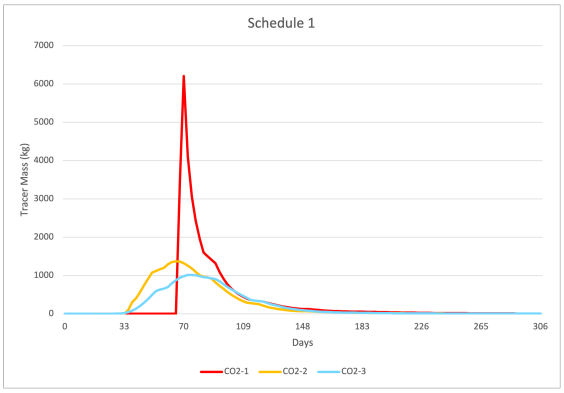


**(a)** Schedule 1

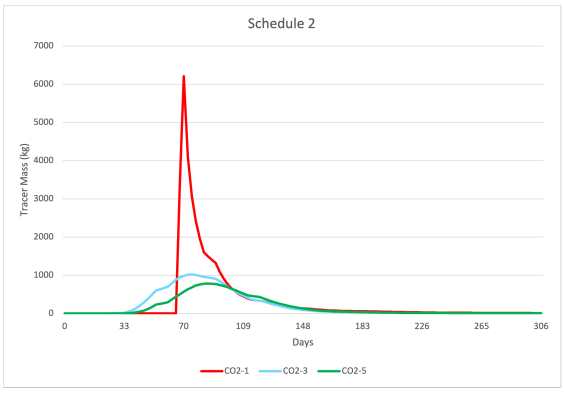


**(b)** Schedule 2

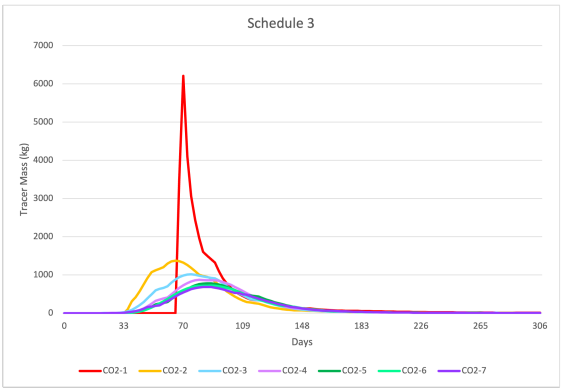


**(c)** Schedule 3

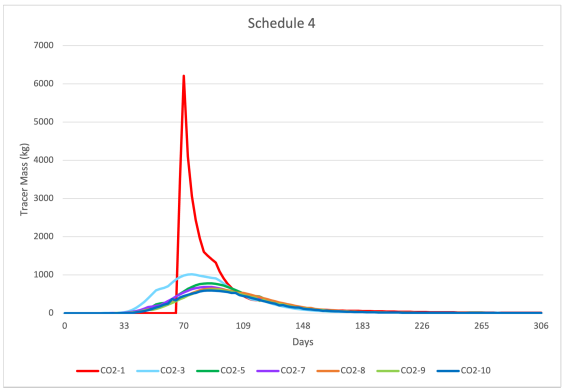


**(d)** Schedule 4

**Figure 4-5:** MODEL 2: Tracer breakthrough curves for Schedules 1-4

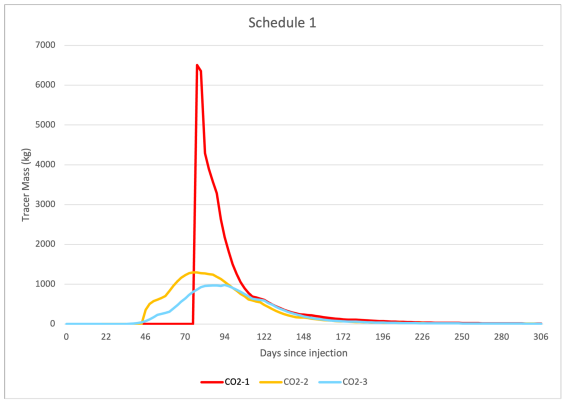


**(a)** Schedule 1

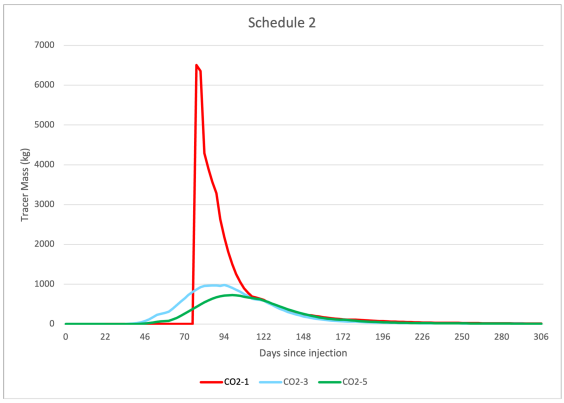


**(b)** Schedule 2

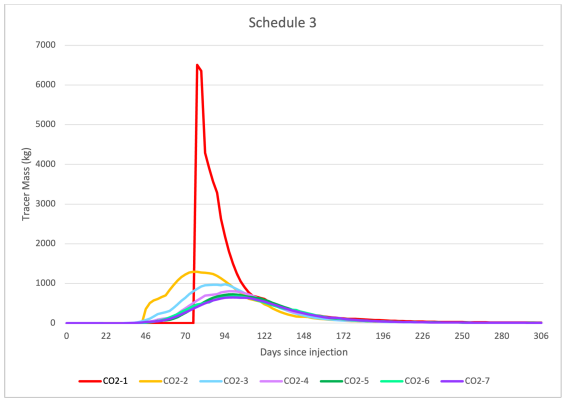


**(c)** Schedule 3

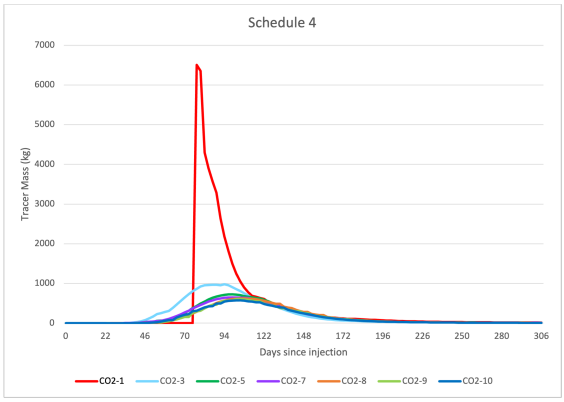


**(d)** Schedule 4

**Figure 4-6:** MODEL 3: Tracer breakthrough curves for Schedules 1-4

Below we visualize the gas saturation in Model 1, Model 2, and Model 3 after 3.5 years. Model 1 possesses a high permeability range, as previously mentioned. Model 2 possesses a lower permeability range, and Model 3 is homogeneous. In the homogeneous case the largest amount of the reservoir is swept.

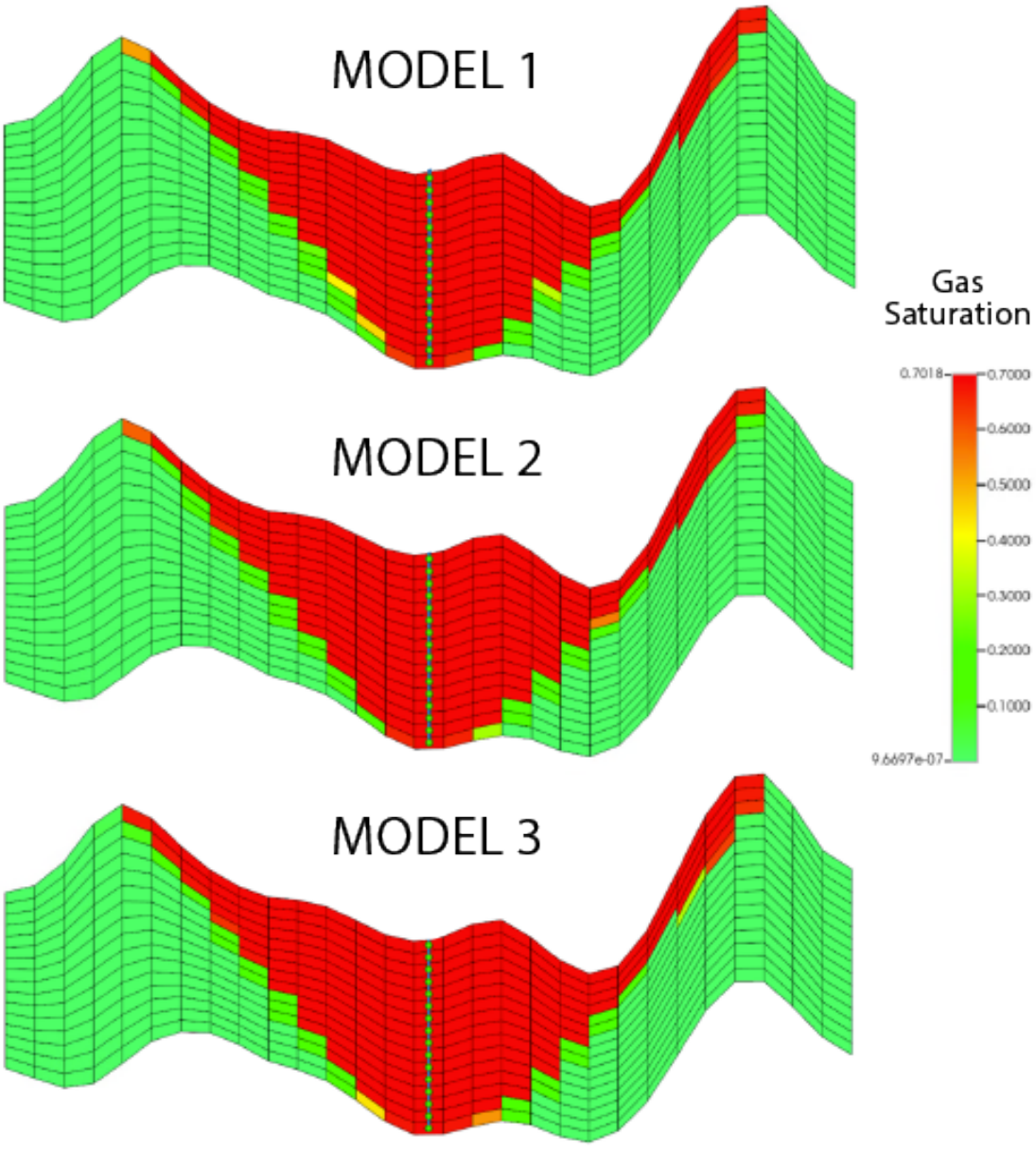


**Figure 4-7:** Gas saturation after 3.5 years. Cross section intersects the injection well.

Below we visualize the tracer breakthrough of 1 kg for $CO_2$-1 - 10 and the corresponding table of values. Initial breakthrough of the tracer is highly variable ($8.10 * 10^{-43}$ - $9,612$ kg), so the breakthrough time of 1 kg of each tracer was chosen to standardize the recovered quantities.

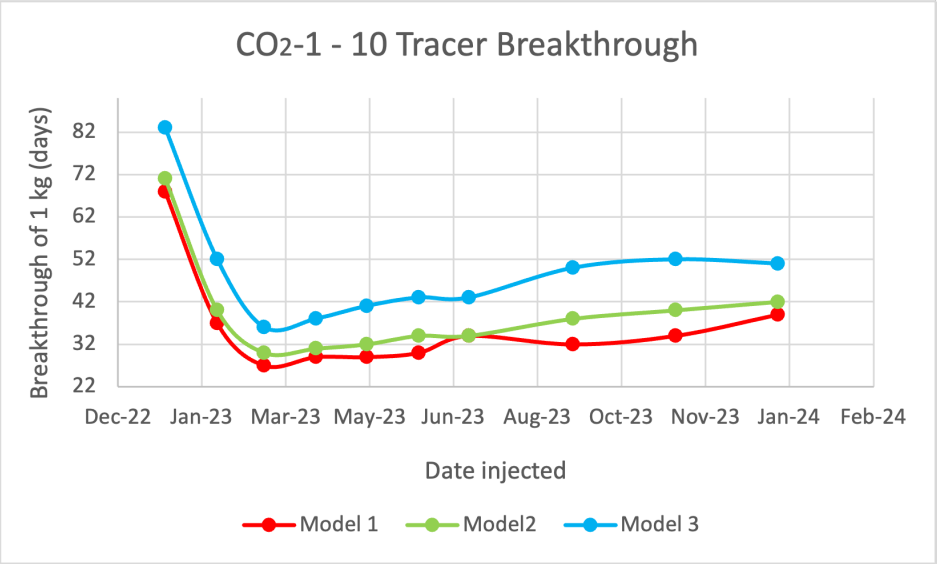


**Figure 4-8:** $CO_2$ breakthrough for each tracer

| $CO_2$ Tracer Breakthrough (days) | | | | | | | | | | |
|---|---|---|---|---|---|---|---|---|---|---|
| | $CO_2$-1 | $CO_2$-2 | $CO_2$-3 | $CO_2$-4 | $CO_2$-5 | $CO_2$-6 | $CO_2$-7 | $CO_2$-8 | $CO_2$-9 | $CO_2$-10 |
| 1 | 68 | 37 | 27 | 29 | 29 | 30 | 34 | 32 | 34 | 39 |
| 2 | 71 | 40 | 30 | 31 | 32 | 34 | 34 | 38 | 40 | 42 |
| 3 | 83 | 52 | 36 | 38 | 41 | 43 | 43 | 50 | 52 | 51 |

**Table 4-1:** $CO_2$ breakthrough of 1 kg for each tracer in Model 1, Model 2, and Model 3

# Chapter 5

# Discussion

## 5-1 Tracer Interpretation

Upon first examination of the tracer breakthrough curves for Schedule 1-4 and for Model 1, Model 2, Model 3 (Figure 4-4, Figure 4-5, Figure 4-6), it is evident that tracer $CO_2$-1 (red) is an outlier. Tracer $CO_2$-1 does not reflect tracer recovery mid-production like the other tracers, but rather, it reflects the breakthrough of $CO_2$. Because of this, the curve has a sharp breakthrough front, occurring 68, 71, and 83 days after injection for Model 1, Model 2, and Model 3, respectively. The sharp breakthrough corresponds to the front of the injected fluid, $CO_2$. The time of the front breakthrough, represented by $CO_2$-1, deviates from the initial breakthrough of the other tracers which have a breakthrough time between 1 to 24 days after injection. For a recovery of 1 kg of tracer tracers $CO_2$-2 - 10 have a breakthrough time between 27 to 52 days. This difference in breakthrough time is clearly evidenced by the lag of tracer $CO_2$-1 compared to tracers $CO_2$-2 - 10. Due to the exceptional nature of tracer $CO_2$-1, we will not discuss its recovery in the context of the other tracers extensively.

### 5-1-1 Heterogeneity

We first examine the effects of heterogeneity in Figure 4-7. Here, the $CO_2$ plume has reached steady state after 3.5 years in each of the three models. In Model 3, the homogeneous case, the largest amount of the reservoir is swept. In Model 1, the high-permeability range case, the smallest amount of the reservoir is swept. This occurs as $CO_2$ migrates towards the upper, more permeable layers. Thus, sweep is greatest in the homogeneous case.

We can also visualize the impacts that heterogeneity has on the breakthrough curves in Figure 4-2. Model 1 produces a high recovery of tracer $CO_2$-1, exceeding 9,000 kg in a day. This high recovery in Model 1 may be attributed to the larger permeability range which forces $CO_2$ to migrate upwards, as is already its nature, leading to such a sharp peal and more rapid recovery. However, the trend does not continue in Model 2 as the breakthrough amplitude of $CO_2$-1 is approximately the same as that of Model 3.

Faster tracer breakthrough of the heterogeneous cases can also be visualized in Figure 4-8. Model 3 has larger breakthrough times compared to the heterogeneous cases. We hypothesize that in the heterogeneous case, the permeability gradient forces $CO_2$ to migrate upwards leading to faster initial breakthrough of the tracer. In the homogeneous case, however, uniform permeability permits greater flow of $CO_2$ at greater depths in the reservoir. Because breakthrough occurs after the longest amount of time in the homogeneous case, here we would also have a larger sweep. This was previously confirmed by the gas saturation models in Figure 4-7.

One feature that is surprising is that tracer breakthrough takes the longest initially, decreases, and then increases again. This behavior is visualized in Figure 4-8. The long tracer breakthrough for the first two tracers, $CO_2$-1 and $CO_2$-2 (83 and 53 days, respectively) might be associated with low mobility of the $CO_2$ in the presence of water. Once $CO_2$ gas saturation of the reservoir improves, $CO_2$ tracer breakthrough time falls (27 - 36 days for $CO_2$-3) and residence time decreases. As the plume grows, sweep improves, and residence times increase. This is demonstrated by the linearly increasing trend in Figure 4-8.

From this figure, however, we can definitively take away that increasing heterogeneity is associated with shorter breakthrough times and poorer sweep. The homogeneous model possesses the longest breakthrough time and the best sweep of the three models.

### 5-1-2 Injection interval

The importance of this parameter comes into play especially when determining early recovery. Between the recovery of $CO_2$-1 (red) and $CO_2$-3 (blue) in Schedule 2 a lot of information is lost regarding the distribution of tracer recovery and, therefore, early stages of sweep. Thus, a two-month injection interval (dt=2) is not recommended for an early-stage tracer program (Schedule 2,4). Schedules 1 and 4 implement a one-month injection interval (dt=1) and provide more information just after the initial injection and breakthrough of $CO_2$ at the producer. However, there is still a big change between $CO_2$-1 and $CO_2$-2, indicating a dramatic change in sweep during this month between injection of $CO_2$-1 and $CO_2$-2. On long-time scales, the interval between tracer injections (dt) does not impact the recovery trend. We observe in Schedule 3 and 4 that tracers visually converge toward the curve of $CO_2$-10 for both schedules. For different reservoirs of interest, similar simulations, such as used in this study, should be run to identify a suitable injection interval for determining $CO_2$ plume development and convergence for that site.

### 5-1-3 Number of tracers

With more data we can obtain more information. The more tracers we inject and recover, the greater we can determine the behavior of a $CO_2$ plume over time. We observe in Schedule 3 and 4 that tracers visually converge toward the curve of $CO_2$-10. This convergence represents the stabilization of temporal moment and, therefore, sweep. With only three tracers (N=3) the stabilization of the sweep cannot be determined over a long period of time. This is certainly not possible if one of the tracers used is injected in the initial front. Thus, it is recommended to utilize at least four tracers (N=4) to determine $CO_2$ plume development. For different areas of reservoirs of interest, similar simulations should be run to identify a

suitable number of tracers for determining $CO_2$ plume development and convergence for that site.

### 5-1-4 Sampling duration

In the field it is necessary to sample for long enough to recover the peak and some of the exponential decay of the last tracer injected. The part of a breakthrough curve before the peak demonstrates the conformance of sweep more so than the part of a breakthrough curve after the peak. In Figure 5-1 we see exponential decay of all tracers, occurring after the peak. This provides little information on the evolution of a $CO_2$ plume. However, the part of a breakthrough curve before the peak shows evolution of tracer recovery and, therefore, the plume. As tracers spend more time in the reservoir, sweep increases. Thus, in the field tracers must be sampled long enough to recover the peak and a portion of the exponential decay of the last tracer to extract information on plume evolution.

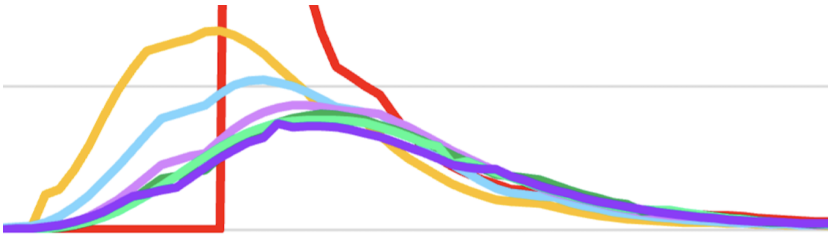

**Figure 5-1:** Conformance of sweep from Model 1, Schedule 3

### 5-1-5 Tracer quantity

Recommendations for tracer quantity were previously made in subsection 2-2-7 but are re-stated here. Due to the low detection limits of PFTs (200 parts per quadrillion), it is not necessary for a large quantity of the tracer to be injected. Soltanian et al. injected 5.2 kg of PFT over two hours. Freifeld et al. injected 3 kg of PFT over five hours. McCallum et al. injected 4 kg of PFT over five hours. Therefore, we recommend injecting 5 kg PFT over 5-6 hours for a well spacing of 1 km.

# Chapter 6

# Conclusion

Tracer campaigns performed during a field demonstration can provide information on how a $CO_2$ plume evolves over time which may be extrapolated in time and space for application of long-term, large-scale heat recovery for commercial CPG. In this study we aimed to answer the following question,

> **How does varying the tracer injection interval (dt) and the number of tracers (N) in three reservoir models affect the determination of $CO_2$ plume development? What are the optimal tracer field campaign recommendations based on these reservoir simulations?**

In order to enhance sweep efficiency assessments and provide tracer field campaign recommendations, we use tagged $CO_2$ tracers in reservoir simulations of the Utsira formation in the Sleipner field. We found that the determination of $CO_2$ plume development and sweep conformance was optimized using 7 tracers (N=7) in one-month intervals (dt=1) in our reservoir. Additionally, we found that our homogeneous model possesses the largest sweep of the three models, as a uniform permeability permits greater flow of $CO_2$ at greater depths in the reservoir. Based on our results, we recommend injecting 35 kg (5 kg each) of 7 perfluorocarbon tracers (PFT) over 5-6 hours in one-month intervals. However, for different areas reservoirs of interest, similar simulations, such as used in this study, should be run to identify a suitable number of tracers and a suitable injection interval(s) for determining $CO_2$ plume development and convergence for that site. We recommend sampling in the field using the Agilent 6890N gas chromatograph until recovery of the peak and a portion of the exponential decay of the last tracer for optimal determination of $CO_2$ plume development. From our findings, a tracer campaign would help reduce uncertainty in modelling, predictions and history-matching, and improve understanding of sweep efficiency and long-term heat recovery. Below we summarize the findings of this study and opportunities for further research.

## 6-1 Tracer Interpretation

Three models were tested: Model 1, Model 2, and Model 3. Model 1 has a permeability range of 2750 - 1250 mD, Model 2 has a range of 2500 - 1500 mD, and Model 3 has a constant permeability of 2000 mD. We found that increasing heterogeneity is associated with shorter breakthrough times and poorer sweep. The homogeneous model possesses the longest breakthrough time and the best sweep of the three models.

## 6-2 Tracer Campaign Recommendation

### 6-2-1 Tracer selection

The use of Perfluorocarbon tracers (PFT) are recommended for the purpose of a field campaign. Perfluorocarbons are highly stable, conservative, chemically inert, inexpensive, and detectable at low limits (200 parts per quadrillion). Common PFTs include perfluoromethylcyclopentane (PMCP), perfluorodimethylcyclobutane (PDMCB), perfluoromethylcyclohexane (PMCH), but there exists a wide range of commercially available cyclic PFTs (Myers et al., 2013). Multiple PFTs may be used in a single study to determine the evolution of tracer recovery and plume development.

### 6-2-2 Tracer schedule

If a tracer is injected during the initial injection of $CO_2$, it is recommended to utilize at least three more tracers (N=4) to determine $CO_2$ plume development. Utilizing 7 tracers (N=7) in one-month intervals (dt=1) was ideal for the Sleipner field, but tracer schedule recommendations will depend on the reservoir of interest. A recommended schedule would utilize more tracers in early stages of $CO_2$ injection and less tracers in late stages, as sweep increases rapidly in the early stages of $CO_2$ injection. For different reservoirs of interest, similar simulations such as used in this study should be run to identify a suitable number of tracers and a suitable injection interval(s) for determining $CO_2$ plume development and convergence for that site. Tracers must also be sampled long enough to recover the peak and a portion of the exponential decay of the last tracer for interpretation.

### 6-2-3 Tracer quantity

Due to the low detection limits of PFTs (200 parts per quadrillion), it is not necessary for a large quantity of the tracer to be injected. Soltanian et al. injected 5.2 kg of PFT over two hours. Freifeld et al. injected 3 kg of PFT over five hours. McCallum et al. injected 4 kg of PFT over five hours. Therefore, we recommend injecting 5 kg PFT over 5-6 hours for a well spacing of 1 km.

### 6-2-4 Sample collection

The method described previously in subsection 2-2-7 should be employed for tracer sample collection. The Agilent 6890N gas chromatograph can be used in the field. A pressure

regulator connected by valves to the gas chromatograph is necessary to lower the pressure of the sample taken from the well. Valves should be computer-controlled to allow for the automation of sampling. An additional sample will also allow for samples to be collected for lab analysis and comparison with field measurements. In the field tracers must be sampled long enough to recover the peak and a portion of the exponential decay of the last tracer to extract information on plume evolution.

### 6-2-5 Further Research

The following opportunities for further research are identified here.

[1] Further studies could quantify $CO_2$ sweep in reservoir simulations and relate this to recovered tracer profiles.

[2] An opportunity for further work could be to utilize a synthetic (hidden) model for history-matching the plume shape using tracer data.

[3] Further research could measure how reservoir parameters impact tracer recovery, and further, long-term heat recovery. Parameters such as temperature-depth, pressure-depth, relative permeability curves, porosity, and permeability may be more systematically varied to determine how they impact sweep efficiency in different reservoirs.

[4] Further studies could model Perfluorocarbon tracers directly in CMG using the properties listed in Figure 6-1. The tracers may be defined by their molecular weight in the component property sections. This is upon recommendation from the Computer Modelling Group Ltd. (CMG) Technical Support Team. Email correspondence is seen in Figure 6-2.

**TABLE 6.6—PROPERTIES OF THE MOST FREQUENTLY APPLIED PERFLUOROCARBON GAS TRACERS (after Dugstad[11])**

| Perfluorocarbons Tracer | Abbreviation | Chemical Formula | Molecular Weight | Boiling Point |
|---|---|---|---|---|
| Perfluoromethylecyclopentane | PMCP | $C_6F_{12}$ | 300 | 48 |
| Perfluorodimethylcyclobutane | PDMCB | $C_6F_{12}$ | 300 | 45 |
| Perfluoromethylecyclohexane | PMCH | $C_7F_{14}$ | 350 | 76 |
| 1,3 Perfluorodimethylcyclohexane | 1,3-PDMCH | $C_8F_{16}$ | 400 | 102 |

**Figure 6-1:** Properties of Perfluorocarbon gas tracers (Dugstad, 1992).

Hello,

Further to below. There is no specific option for " perfluorocarbon" gas tracer. However, by using the tracer specification keywords, one can specify the properties of the tracer gas, like its molecular weight, which would be used by the simulator. Hence, with these keywords one can mimic the perfuorocarbon properties, even if a direct specification of perfluorocarbon is not available.

## Tracer Definition (Optional)

**PURPOSE:**

These keywords are used to define passive tracers and assign their associate components that are used to track the movemenent of the components of interest in a simulation

**FORMAT:**

| | |
|---|---|
| *NTRCR | $n\_trc$ |
| *TRCRNAME | $cname\_trc$ |
| *MW-TRCR | $mw\_trc$ |
| *TRCR-ASSOC $\{cname\_assoc_i$ | $cname\_trc_{itrc}, cname\_trc_{jtrc}, \ldots, \ldots\}$ |

**Figure 6-2:** CMG email regarding Perfluorocarbon tracers

# Bibliography


Adams, B. M., Kuehn, T. H., Bielicki, J. M., Randolph, J. B., and Saar, M. O. (2014). On the importance of the thermosiphon effect in CPG (CO2 plume geothermal) power systems. *Energy*, 69:409–418.

Adams, B. M., Kuehn, T. H., Bielicki, J. M., Randolph, J. B., and Saar, M. O. (2015a). A comparison of electric power output of CO2 Plume Geothermal (CPG) and brine geothermal systems for varying reservoir conditions. *Applied Energy*, 140:365–377.

Adams, B. M., Kuehn, T. H., Bielicki, J. M., Randolph, J. B., and Saar, M. O. (2015b). A comparison of electric power output of CO2 Plume Geothermal (CPG) and brine geothermal systems for varying reservoir conditions. *Applied Energy*, 140:365–377.

Adams, B. M., Kuehn, T. H., Randolph, J., and Saar, M. O. (2013). The reduced pumping power requirements from increasing the injection well fluid density. *Geothermal Resources Council (GRC) Transactions*, 37.

Akervoll, I., Lindeberg, E., and Lackner, A. (2009). Feasibility of Reproduction of Stored CO2 from the Utsira Formation at the Sleipner Gas Field. *Energy Procedia*, 1(1):2557–2564.

Albarado, S. and Grajeda, A. (2023). Arkansas Advocate, Tornadoes kill at least 5 in Arkansas, damage hundreds of homes and businesses, Outpouring of support energizes recovery effort.

Alnes, H., Eiken, O., Nooner, S., Sasagawa, G., Stenvold, T., and Zumberge, M. (2011). Results from Sleipner gravity monitoring: Updated density and temperature distribution of the CO2 plume. In *Energy Procedia*, volume 4, pages 5504–5511. Elsevier Ltd.

Anderson, M. P. (2005). Heat as a Ground Water Tracer. *Groundwater*, 43(6):951–968.

Blaushild, D. (2015). Collection and Analysis of Perfluorocarbon Tracer Compounds. In *National Energy Technology Laboratory*. U.S. Department of Energy.

Bratvold, R. B., Bickel, J. E., and Lohne, H. P. (2007). Value of Information in the Oil and Gas Industry: Past, Present, and Future. In *SPE Annual Technical Conference and Exhibition*. Society of Petroleum Engineers.

Brigham-Grette, J., Melles, M., Minyuk, P., Andreev, A., Tarasov, P., and DeConto, R. (2013). Pliocene Warmth, Polar Amplification, and Stepped Pleistocene Cooling Recorded in NE Arctic Russia. *Science*, 340.

Cao, V., Schaffer, M., Taherdangkoo, R., and Licha, T. (2020). Solute Reactive Tracers for Hydrogeological Applications: A Short Review and Future Prospects. *Water*.

CMG Ltd. (2022). CMG, CO2 Sequestration Modelling using GEM. Technical report.

CO2DataShare/CSDC, S. and Equinor (2020). Sleipner 2019 Benchmark Model - Datasets - CO2DataShare.

De Reus, A. J., Karpan, V., Van Batenburg, D. W., and Mikhaylenko, E. (2019). Mo A 08 Use of Tracers in the Alkaline-Surfactant-Polymer Pilot in West Salym. EAGE, 20th European Symposium on Improved Oil Recovery.

DeMillo, A. (2023). PBS, Tornadoes slam Arkansas, shredding homes and tossing cars.

Dugstad, O. (1992). An experimental study of tracers for labelling of injection gas in oil reservoirs. Technical report, University of Bergen, Norway.

Dumitru, O. A., Austermann, J., Polyak, V. J., Fornós, J. J., Asmerom, Y., Ginés, J., Ginés, A., and Onac, B. P. (2019). Constraints on global mean sea level during Pliocene warmth. *Nature*, 574:233–236.

EarthHow (2022). How the Greenhouse Effect Traps Heat and Warms Earth.

Equinor (2020). 25 years of successful offshore CO storage in Norway. Technical report, Equinor.

Equinor ASA (2023). Equinor, The Northern Lights Project.

European Parliament (2009). Directive 2009/31/EC of the European Parliament and of the Council on the geological storage of carbon dioxide and amending Council Directive 85/337/EEC, European Parliament and Council Directives 2000/60/EC, 2001/35/EC, 2006/12/EC, 2008/1/EC and Regulation (EC) No 1013/2006. *Official Journal of the European Union*, 26:158–179.

Fleming, M. R., Adams, B. M., Kuehn, T. H., Bielicki, J. M., and Saar, M. O. (2020). Increased Power Generation due to Exothermic Water Exsolution in CO2 Plume Geothermal (CPG) Power Plants. *Geothermics*, 88.

Fonseca, X., Miguez-Macho, G., Cortes-Vazquez, J. A., and Vaamonde, A. (2022). A physical concept in the press: the case of the jet stream. *Geoscience Communication*, 5(3):177–188.

Freifeld, B. M., Trautz, R. C., Kharaka, Y. K., Phelps, T. J., Myer, L. R., Hovorka, S. D., and Collins, D. J. (2005). The U-tube: A novel system for acquiring borehole fluid samples from a deep geologic CO2 sequestration experiment. *Journal of Geophysical Research: Solid Earth*, 110(10):1–10.

Frost, E. (1946). Helium Tracer Studies in the Elk Hills, California, Field. Technical report, US Bureau of Mines.

GEG Group (2023a). AEGIS-CH Insights – Geothermal Energy and Geofluids, ETH Zürich, Switzerland.

GEG Group (2023b). CPG Technology – Geothermal Energy and Geofluids, ETH Zürich, Switzerland.

Gilfillan, S. M., Wilkinson, M., Haszeldine, R. S., Shipton, Z. K., Nelson, S. T., and Poreda, R. J. (2011). He and Ne as tracers of natural CO2 migration up a fault from a deep reservoir. *International Journal of Greenhouse Gas Control*, 5(6):1507–1516.

Goni, I. B. (2006). Tracing stable isotope values from meteoric water to groundwater in the southwestern part of the Chad basin. *Hydrogeology Journal*, 14(5):742–752.

Hamilton, J. G. (1942). The Use of Radioactive Tracers in Biology and Medicine1. *Radiology*, 39(5):541–572.

Hassoun, S., McBride, T., and Russell, D. A. (2000). Development of perfluorocarbon tracer technology for underground leak location. *Journal of Environmental Monitoring*, 2(5):432–435.

Hermanrud, C., Andresen, T., Eiken, O., Hansen, H., Janbu, A., Lippard, J., Bolås, H. N., Simmenes, T. H., Teige, G. M. G., and Østmo, S. (2009). Storage of CO2 in saline aquifers-Lessons learned from 10 years of injection into the Utsira Formation in the Sleipner area. In *Energy Procedia*, volume 1, pages 1997–2004.

Holloway, S., Chadwick, R., Kirby, G., Pearce, J., Gregersen, U., Johannessen, P., Kristensen, L., Zweigel, P., Lothe, A., and Arts, R. (2000). Saline Aquifer CO2 Storage (SACS) - Final Report: work area 1 (Geology. BGS report, 31 pp, in confidence.). Technical report, SINTEF.

International Energy Agency (IEA) (2023). CO2DataShare.

Kantzas, A., Bryan, J., and Taheri, S. (2023). *Fundamentals of Fluid Flow in Porous Media*. PERM Inc. Special Core Analysis & Enhanced Oil Recovery Laboratory, Calgary.

Kong, X. Z., Deuber, C. A., Kittilä, A., Somogyvári, M., Mikutis, G., Bayer, P., Stark, W. J., and Saar, M. O. (2018). Tomographic Reservoir Imaging with DNA-Labeled Silica Nanotracers: The First Field Validation. *Environmental Science and Technology*, 52(23):13681–13689.

Kong, X. Z. and Saar, M. O. (2013). Numerical study of the effects of permeability heterogeneity on density-driven convective mixing during CO2 dissolution storage. *International Journal of Greenhouse Gas Control*, 19:160–173.

Leinbundgut, C. and Seibert J (2011). *Tracer Hydrology. In: Peter Wilderer (ed.) Treatise on Water Science*, volume 2. Oxford: Academic Press.

Levenspiel, O. (1972). *Chemical Reaction Engineering*. John Wiley and Sons, New York, 2nd edition.

Lindeberg, E. and Holt, T. (2000). Saline Aquifer CO 2 Storage (SACS): Task 2: Fluid and core properties and reservoir simulation. Technical report, SINTEF, TNO.

Ljosland, E., Bjornstad, T., Dugstad, O., and Hundere, I. (1993). Perfluorocarbon tracer studies at the Gullfaks field in the North Sea. *Journal of Petroleum Science and Engineering*, 10:27–38.

Lothe, A. and Zweigel, P. (1999). Saline Aquifer CO2 Storage (SACS). Informal annual report 1999 of SINTEF Petroleum Research result in work area 1: Reservoir Geology. Technical report, SINTEF.

Lu, J., Cook, P. J., Hosseini, S. A., Yang, C., Romanak, K. D., Zhang, T., Freifeld, B. M., Smyth, R. C., Zeng, H., and Hovorka, S. D. (2012). Complex fluid flow revealed by monitoring CO2 injection in a fluvial formation. *Journal of Geophysical Research: Solid Earth*, 117(3).

Luhmann, A. J., Covington, M. D., Alexander, S. C., Yi Chai, S., Schwartz, B. F., Groten, J. T., and Calvin Alexander Jr, E. (2012). Comparing conservative and nonconservative tracers in karst and using them to estimate flow path geometry. *Journal of Hydrology*.

McCallum, S., Riestenberg, D., Cole, D., Freifeld, B., Trautz, R., Hovorka, S., and Phelps, T. (2005). Monitoring Geologically Sequestered CO2 during the Frio Brine Pilot Test using Perfluorocarbon Tracers: presented at the National Energy Technology Laboratory Fourth Annual Conference on Carbon Capture and Sequestration. pages 1–9, Alexandria, Virginia. GCCC Digital Publication.

Melo, C. L., Bressan, L. W., Ketzer, J. M. M., Constant, M. J., and Cristina de Castro Araujo Moreira, A. (2014). Study of gas tracers for CO2 monitoring. *Energy Procedia*, 63:3864–3868.

Metz, B., Davidson, O., de Coninck, H., Loos, M., and Meyer, L. (2005). IPCC Special Report on Carbon Dioxide Capture and Storage. Prepared be Working Group III of the Intergovernmental Panel on Climate Change. Technical report, Cambridge University Press, Cambridge, United Kingdom and New York, USA.

MIT (2015). Sleipner Fact Sheet: Carbon Dioxide Capture and Storage Project.

Myers, M., Stalker, L., Pejcic, B., and Ross, A. (2013). Tracers - Past, present and future applications in CO2 geosequestration. *Applied Geochemistry*, 30:125–135.

NASA Earth Science Communications Team (2023). NASA, Why Is Carbon Important?

Nooner, S. L., Eiken, O., Hermanrud, C., Sasagawa, G. S., Stenvold, T., and Zumberge, M. A. (2007). Constraints on the in situ density of CO 2 within the Utsira formation from time-lapse seafloor gravity measurements. *International Journal of Greenhouse Gas Control*, pages 198–214.

Norouzi, A. M., Gluyas, J., and Babaei, M. (2022). CO2-plume geothermal in fluvial formations: A 2D numerical performance study using subsurface metrics and upscaling. *Geothermics*, 99.

Olalotiti-Lawal, F., Tanaka, S., and Datta-Gupta, A. (2020). Streamline-Based Simulation of Carbon Dioxide Sequestration in Saline Aquifers. Technical report.

Pacala, S. and Socolow, R. (2004). Stabilization Wedges: Solving the Climate Problem for the Next 50 Years with Current Technologies. *Science*, 305.

Patidar, A. K., Joshi, D., Dristant, U., and Choudhury, T. (2022). A review of tracer testing techniques in porous media specially attributed to the oil and gas industry. *Journal of Petroleum Exploration and Production Technology*, 12(12):3339–3356.

Pham, V. T. H., Riis, F., Gjeldvik, I. T., Halland, E. K., Tappel, I. M., and Aagaard, P. (2013). Assessment of CO 2 injection into the south Utsira-Skade aquifer, the North Sea, Norway. *Energy*, 55:529–540.

Pruess, K. (2006). Enhanced geothermal systems (EGS) using CO2 as working fluid-A novel approach for generating renewable energy with simultaneous sequestration of carbon. *Geothermics*, 35(4):351–367.

Pruess, K. (2007). Role of Fluid Pressure in the Production Behavior of Enhanced Geothermal Systems with CO 2 as Working Fluid. Technical report, Lawrence Berkeley National Lab, Berkeley, California (USA).

Randolph, J., Adams, B. M., Zurich, E., and Kuehn, T. H. (2012). Wellbore heat transfer in CO2-based geothermal systems. *GRC Transactions*, 36:549.

Randolph, J. B. and Saar, M. O. (2011a). Combining geothermal energy capture with geologic carbon dioxide sequestration. *Geophysical Research Letters*, 38(10).

Randolph, J. B. and Saar, M. O. (2011b). Coupling carbon dioxide sequestration with geothermal energy capture in naturally permeable, porous geologic formations: Implications for CO2 sequestration. *Energy Procedia*, 4:2206–2213.

Randolph, J. B. and Saar, M. O. (2011c). Coupling carbon dioxide sequestration with geothermal energy capture in naturally permeable, porous geologic formations: Implications for CO2 sequestration. In *Energy Procedia*, volume 4, pages 2206–2213. Elsevier Ltd.

Ren, Y., Kong, Y., Pang, Z., and Wang, J. (2023). A comprehensive review of tracer tests in enhanced geothermal systems. *Renewable and Sustainable Energy Reviews*, 182.

Resman Energy Technology (2022). RESMAN Interwell Tracer Technology (Youtube).

Schlumberger Limited. (2023). Schlumberger Energy Glossary.

Senum, G., Faker, R., DeRose, W., Harris, B., and Ottaviani, W. (1992). Petroleum Reservoir Characterization by Perfluorocarbon Tracers. In *Eighth Symposium on Enhanced Oil Recovery*, Tulsa, Oklahoma (USA). Society of Petroleum Engineers (SPE), US Department of Energy (DOE).

Shannon, G. and Bielicki, J. (2021). CO2 Plume Geothermal (CPG) Video.

Shook, G. M. and Forsmann, J. H. (2005). Tracer Interpretation Using Temporal Moments on a Spreadsheet. Technical report, Idaho National Laboratory, Idaho Falls, Idaho.

SINTEF (2019). Sleipner CO2 Reference Dataset License Terms.

Soltanian, M. R., Amooie, M. A., Cole, D., Graham, D., Pfiffner, S., Phelps, T., and Moortgat, J. (2018). Transport of perfluorocarbon tracers in the Cranfield Geological Carbon Sequestration Project. *Greenhouse Gases: Science and Technology*, 8(4):650–671.

Spycher, N. and Pruess, K. (2010). A Phase-partitioning model for CO2-brine mixtures at elevated temperatures and pressures: Application to CO2-enhanced geothermal systems. *Transport in Porous Media*, 82(1):173–196.

Spycher, N., Pruess, K., and Ennis-King, J. (2003). CO2-H2O mixtures in the geological sequestration of CO2. I. Assessment and calculation of mutual solubilities from 12 to 100°C and up to 600 bar. *Geochimica et Cosmochimica Acta*, 67(16):3015–3031.

Stein, T. (2022). National Oceanic and Atmospheric Administration, Carbon dioxide now more than 50% higher than pre-industrial levels.

Towler, B. F. (2014). *The Future of Energy*. Academic Press (Elsevier Inc.), London, 1 edition.

Treisman, R. (2023). NPR, Climate, The exact link between tornadoes and climate change is hard to draw. Here's why.

University of Calgary (2023). Geothermal gradient - Energy Education.

Wagner, O. R. (1977). The Use of Tracers in Diagnosing Interwell Reservoir Heterogeneities - Field Results. *Jounral of Petroleum Technology*.

Wellmann, F. and Caumon, G. (2018). 3-D Structural geological models: Concepts, methods, and uncertainties. *Advances in Geophysics*, 59:1–121.

Wiki Authors (2023). Tornado Alley.

Wilcox, J., Campbell, P., Williamson, P., Beuttler, C., Charles, L., and Wurzbacher, J. (2019). The Role of Direct Air Capture in Mitigation of Anthropogenic Greenhouse Gas Emissions. *Frontiers in Climate — www.frontiersin.org*, 1(10).

Zweigel, P., Lothe, A., Arts, R., and Hamborg, M. (2000). Reservoir geology of the storage units in the Sleipner CO2 injection case - A contribution to the Saline Aquifer CO2 Storage (SACS) project. Technical report, SINTEF.

# Appendix A

# Shook's Method

August 8, 2023

Shook's method derives the first temporal moment in order to calculate swept volume. This method requires density to be constant, which is suitable for water-based tracers. However, supercritical $CO_2$ has highly variable density which depends on temperature, pressure, and depth. Thus, Shook's method cannot be utilized in our case. However, it could be useful to do a water tracer analysis as a pre-flush and compare the results with those from the $CO_2$ tracers.

The mean residence time is the single most useful property from a tracer test (Shook and Forsmann, 2005). The mean residence time is defined as the time it takes to recover half of the total recovered tracer mass. From this time, many properties may be derived. An example of the application of this method is seen in De Reus et al. (2019) where an Alkaline-Surfactant-Polymer pilot was undertaken in West Salym, Russia. In order to use Shook's method, a few conditions must be met,

- steady state injection and extraction
- ideal tracer
- conservative tracer

In order to most accurately analyze the first temporal moment of the tracer recovery, certain steps must be undertaken.

1. correct the tracer recovery for thermal decay
2. normalize the tracer history
3. deconvolve the output signal
4. extrapolate the history to late time
5. calculate the mean residence time and swept volume
6. calculate the flow geometry

We describe a few of these steps here, but for more detail, the reader is directed to (Shook and Forsmann, 2005).

## A-1 Correcting for Thermal Decay

This correction is most commonly completed using the Arrhenius equation,

$$k = A * e^{\frac{E_a}{RT}} \tag{A-1}$$

.

where $k$ is the decay constant, $A$ is the pre-exponential factor, $E_a$ is the activation energy, $R$ is the universal gas constant, and $T$ is the temperature ($K$).

However, $k$ is notoriously difficult to calculate as the temperature-depth profile is often poorly constrained. Thus, there is some uncertainty associated with this parameter.

## A-2 Normalizing the Concentration History

The age distribution function $E(t)$ can be calculated as

$$E(t) = \frac{C(t) * \rho * q_{inj}}{M_{inj}} \tag{A-2}$$

where $E(t)$ has units $\frac{1}{day}$, $C(t)$ is the produced tracer concentration $(ppb)$, $\rho$ is the density $(kg/m^3)$, $q_{inj}$ is the volumetric mass injection rate $(\frac{m^3}{day})$ and $M_{inj}$ is the mass of the injected tracer $(kg)$.

The age distribution function $(\frac{1}{day})$ is used instead of the recovered tracer concentration $(ppb)$ as often times a tracer is reinjected and the age distribution function better differentiates recovered pulses. Additionally, the use of the age distribution function lends itself to treating the injected tracer as a Dirac delta pulse which is necessary in order to later deconvolve the signal.

## A-3 Deconvolving the Tracer History

In the case of tracer reinjection, it might be difficult to differentiate individual injections, or slugs. Deconvolution is used to remove the effect of tracer recycling. The following convolution integral is used (Levenspiel, 1972),

$$E_{app}(t) = \int_0^t E_{in}(t-\tau) * E(\tau)\, d\tau \tag{A-3}$$

which states that the observed, or apparent, residence time $E_{app}(t)$ is a product of the injection $E_{in}$ and the true residence time $E(t)$. The $E_{in}$ term assumes an instantaneous injection, represented by the Dirac delta function. The next step is to extrapolate the trace history to long-time, but we do not show that here.

## A-4 Calculating Mean Residence Times

The derived, extrapolated age distribution function is then used to calculate the temporal moment or average mean residence time. This is done using Equation A-4,

$$t^* = \frac{\int_0^\infty E(t) * t\, dt}{\int_0^\infty E(t)\, dt} \tag{A-4}$$

where $t$ is time $(day)$ and $t^*$ is the first temporal moment of a tracer $(day)$.

## A-5 Determining Pore Volume

Lastly, the pore volume ($V_p$), measured in ($m^3$) swept by the tracer can be calculated as follows,

$$V_p = \frac{m}{M_{inj}} * q_{inj} * t^* \tag{A-5}$$

or

$$V_p = \% \text{ of Injected Rate} * \text{Mean transit time} \tag{A-6}$$

where $m$ is the mass of tracer recovered ($kg$), $M_{inj}$ is the mass of tracer injected in the initial pulse injection ($kg$), and $q_{inj}$ is the volumetric injection rate ($\frac{m^3}{day}$). From here, flow geometry may be calculated.